Review

Triplet superconducting correlations in hybrid superconducting junctions.

Karén Y. Constantinian*, Gennady A. Ovsyannikov#, Yulii V. Kislinskii, Andrey M. Petrzhik

Kotel'nikov Institute of Radio Engineering and Electronics Russian Academy of Sciences, Mokhovaya 11–7, Moscow, 125009, Russia

* Correspondence: karen@hitech.cplire.ru, Tel.+74956297431 Karen Y. Constantinian

gena@hitech.cplire.ru, Tel.+74956297431 Gennady A. Ovsyannikov

Abstract: We summarize the results on electron transport in hybrid superconducting S_d/B/S mesa-structure consisted of the oxide epitaxial S_d/B heterostructures, where S_d is the cuprate $YBa_2Cu_3O_{7-\delta}$ superconductor, B – an interlayer with the spin dependent characteristics, and S is the Nb top superconductor. Josephson effect was observed manifested in appearance of oscillating Shapiro steps amplitudes with microwave signal power due to synchronization of junction self-generation of electromagnetic radiation and the external microwave probe signal. Triplet component of superconducting correlations emerged when the interlayer comprised two magnetic materials ruthenate $SrRuO_3$ and manganite $La_{0.7}Sr_{0.3}MnO_3$ with non-collinear magnetizations as well in the case of antiferromagnetic insulator Sr_2IrO_4 characterized by strong spin-orbit interaction. While there is no Josephson effect neither in the case of a single manganite ($La_{0.7}Sr_{0.3}MnO_3$ or $La_{0.7}Ca_{0.3}MnO_3$), nor of the single ruthenate film used as a interlayer. Thickness of the interlayer in the both cases considerably exceeded the coherence length of the magnetic spin active interlayer hinting on appearance of long-range proximity effect and spin-triplet superconducting current. Magnetic field dependences measured at dc, and the existence of the second harmonic in superconducting current–phase relation revealed by measurements at microwave frequencies will be discussed.

Keywords: superconductivity; Josephson effect; hybrid heterostructures; mesa-structure; magnetic proximity effect; triplet pairing; spin-orbit interaction.

1. Introduction

Two decades ago it was theoretically shown that near the interface, composed from ferromagnetic (F) and superconducting materials (S), spin-triplet superconducting correlations with nonzero spin projection may occur [1,2]. A distinctive feature of spin-triplet superconducting correlations is their insensitivity to the magnetic exchange field E_{EX} which usually exceeds the thermal energy k_BT (T is ambient temperature, k_B is the Boltzmann constant) allowing penetration of superconducting correlations into a ferromagnet over much longer distances scaled in depths $\xi_N=(\hbar D/k_BT)½$ as in normal metal N, than the characteristic length $\xi_F=(\hbar D/E_{ex})^{1/2}$ of ferromagnet F, where $D=v_Fl/3$ is the diffusion coefficient, v_F is the Fermi velocity, and l is the mean free path in the dirty limit. It makes spin-triplet superconducting pairing applicable for fabrication of superconducting devises with new functional characteristics. One of possibilities to generate spin-triplet superconducting correlations utilizes the coupling of superconducting electrode trough an interlayer (B) prepared of a ferromagnetic three-layer with spatially non-uniform magnetization in layers [2–4], or in a bilayer [5].

Anomalously long-range superconducting proximity effect was attributed first to generation of long-range triplet superconducting correlations experimentally observed during studies of the Andreev interferometer bridge type device made of Ho film with a spiral magnetization [6], and for a S/F/S structure with the CrO_2 interlayer [7,8] exhibiting superconducting critical current. Further, these findings were confirmed in experimental studies of single-crystalline Co nanowires [9], as well

Preprints (www.preprints.org) | NOT PEER-REVIEWED | Posted: 9 May 2023 doi:10.20944/preprints202305.0597.v1

for S/F/S structures with Heusler alloys [10], and when the magnetic interlayer had spiral magnetization [2]. Long-range spin-triplet superconducting currents were observed also in Josephson junctions in which the composite magnetic layers had non-collinear magnetization, particularly in the case of Co/Ru/Co synthetic antiferromagnet and two outer thin F-layers [11], as well for a ferromagnetic three-layer with Co film [12].

All above-mentioned studies were carried out on samples with a metal or simple oxide layers, such as CrO_2. At the same time functional oxides, exhibiting very wide diversity of material properties which encompasses superconductivity, ferromagnetism, ferroelectricity, semiconducting and metallic behavior [13–17], give opportunities for development of superconducting heterostructures based on oxide thin films, comprising superconducting cuprates, ferromagnetic manganites, ruthenates, iridates with strong spin-orbit interaction (SOI), and interfaces formed from them. Complex oxide perovskites as superconducting cuprates and spin-active magnetic materials used as interlayer barrier offer interesting opportunities. First, exhibiting similar crystal structure, oxide perovskites allow fabrication high quality heterostructures with epitaxially grown layers and interfaces. Second, properly prepared magnetic active oxides could feature magnetic exchange energy – a parameter which can be tuned by means of varying the doping level [18]. Third, but not the last, the critical temperatures of cuprate superconductors is more than an order in magnitude larger than in usual metallic superconductors and performs much greater potential interest for applications in field of superconducting spintronics. Several groups contributed to search of long-range proximity effect which leads to spin-triplet superconducting correlations. In this connection the S/F heterostructures with interfaces made of a singlet superconductor and 100% spin polarized F-ferromagnetic manganite at first sight do not help to generate spin-triplet correlations. However, on one hand the authors of Refs. [19,20] reported on evidence of long-range triplet superconducting correlations based on studies of Andreev reflections in structures with $La_{0.7}Ca_{0.3}MnO_3$ ferromagnetic interlayer. On other hand, experiments on similar structures did not reveal superconducting currents (beyond those transmitted through pinholes) [21,22].

It was proved theoretically that spin triplet superconducting current occurs in a composite ferromagnetic interlayer placed in between of two singlet superconductors. The magnetic interlayer consisting of three or more ferromagnetic layers ensure the conversion of the spin-singlet component of superconducting correlations to the spin-triplet correlations, as well the reverse process also took place [3,23]. The experiments on superconducting niobium structures with a composite Co-containing interlayer confirmed the possibility of such processes, although the questions concerning the mixing of compositions of metal layers remain unanswered [11,24]. The reciprocal effect of triplet superconducting correlations on superconducting characteristics of spin-singlet superconductor was studied in [25,26]. A spin-triplet superconducting current in the structures with a ferromagnetic interlayer, consisting of two ferromagnets F_L/F_R, was predicted for ballistic transport in asymmetric superconducting heterostructures $S/F_L/F_R/S$ (without barriers reducing the transparency) with strongly differing thicknesses or exchange fields of the F_L and F_R ferromagnets [27]. The case of diffuse scattering was studied in [5,28] also showed the existence of spin-triplet superconducting component. Later, it was shown theoretically that the dominant second harmonic in the current–phase relation (CPR) of superconducting current performs the long-range superconducting proximity effect [4, 5,29]. The largest superconducting proximity effect with both the first and second harmonics in CPR was predicted for the case of disorientation of magnetizations of F_L and F_R layers by an angle close to 90° and when a thickness of one of the F-ferromagnets is of order of the coherence length ξ_F. From data on the magnetic field dependence of critical current I_c it was concluded [30] that the second harmonic in CPR dominates in heterostructures if the interlayer is prepared from the magnetically active materials.

In this regard a composite manganite/ruthenate $La_{0.7}Sr_{0.3}MnO_3/SrRuO_3$ (LSMO/SRO) interlayer, exhibiting non-collinear magnetization, looks promising for a triplet type Josephson junction. Indeed, this allowed us to observe for the first time a superconducting current though the composite LSMO/SRO interlayer, consisting of two functional oxides, and confirm the presence of spin-triplet component of the superconducting current [31–36].

 doi:10.20944/preprints202305.0597.v1

Another approach to obtain spin-triplet superconducting correlations is based on usage for the interlayer a material with the strong spin-orbit interaction [37–39]. It was predicted the SOI in ferromagnetic interlayer F_{SO} of S/F_{SO}/S junction results in a pure spin-triplet Cooper pairing state without singlet superconductivity [40–43]. However, this issue still needs to be checked. In theoretical study [44] spin-triplet pairing was predicted also for the case of S/N_{SO}/S junction when ferromagnetic interlayer F_{SO} is replaced by N_{SO} - normal metal with SOI. The S/N_{SO} interface for the case of strong SOI in N_{SO} was analyzed in [45] predicting robust spin-triplet pairing due to proximity effect, which allows observation also the Josephson effect in a S/N_{SO}/S junction.

The most of experimental studies of influence of SOI on characteristics of Josephson junctions were done using superconducting structures where S-electrodes were linked by a topological insulator under layer. An unconventional proximity effect was observed in a superconducting junction with Nb S-electrode contacting to magnetically Fe-doped topological insulator (Fe-Bi_2Te_2Se), and the zero bias conductance peak (ZBCP) with energy bands splitting was observed along with conductance oscillations under influence of microwaves [46]. In [47] it was suggested to replace the topological insulator by a material with SOI pushing on an extensive theoretical and experimental studies. The S/B/S junction with Al S-electrodes and InAs semiconductor B-interlayer was experimental studied in [48] and an asymmetry of interference pattern was observed being discussed under the suggestion of impact of strong SOI. The SOI affected also the superconducting current-phase relation (CPR) which deviates from usual periodicity. Particularly, a 4π-periodic behavior was analyzed for a Josephson junction with semiconductor wire weak link [47]. An unconventional CPR in Josephson junctions topological weak link materials were reported and analyzed in [49,50]. The case of a weak link made of a wire with SOI with 8π-periodic CPR was discussed in [51], in which possibility of appearance of a fractional ½ electron charge was attributed to SOI.

For a material to be utilized for B-interlayer with the strong SOI we choose the 5d transition metal oxide Sr_2IrO_4 [52–55]. This compound is known as a canted antiferromagnetic insulator with the band splitting [56,57]. The intrinsic crystal field with energy ~ 0.4 eV [56] splits the degenerate states of 5d electrons into e_g and t_{2g} bands, and the partially filled t_{2g} band splits into J_{eff}=3/2 and J_{eff}=1/2 due to the strong SOI over the iridium ions. Unconventional properties of Sr_2IrO_4, and the interfaces with other oxides, particularly with the superconducting cuprate, were discussed in [58–63] in sense of opportunities for spin manipulation in a junction with the interlayer material with a weak magnetic moment.

In this review we present results of the comprehensive experimental studies of the both types junctions with spin-active interlayers. The paper is organized as follows, besides the Introduction in Section I, sample fabrication and measurements technique are given in Section II. In Section III with sub-section division we summarize experimental data and discuss the dc and microwave transport properties. Conclusions are given in Section IV.

2. Materials and Methods

Hybrid superconducting heterostructures have been fabricated *in situ* by laser ablation of a cuprate superconductor $YBa_2Cu_3O_{7-\delta}$ (YBCO), known as a d-wave superconductor (S_d), and the interlayer, consisting either of $SrRuO_3$ (SRO) and $La_{0.7}Sr_{0.3}MnO_3$ (LSMO) bilayer, or the Sr_2IrO_4 (SIO) thin epitaxial films. The thicknesses of the films are indicated on caption of Figure 1a. The thicknesses of oxide films were controlled by the number of pulses of excimer Kr-laser with 248 nm wavelength. The bottom YBCO thin film and the composite SRO/LSMO interlayer for heterostructure was deposited at temperatures ranged 700-800°C in an oxygen atmosphere of 0.5-0.7 mbar [31–34]. The SIO thin film interlayer was deposited at the same range of temperatures in pure argon atmosphere with pressure 0.5 mbar [64]. Both, the YBCO S_d film and the composite interlayer were grown with the c-axis perpendicular to the substrate plane [32–35]. The crystalline parameters of the YBCO film in heterostructures with the magnetic-active interlayer were determined using the four-circle x-ray diffractometer, measuring 2θ/ω scans and rocking curves [32,35].

Preprints (www.preprints.org) | NOT PEER-REVIEWED | Posted: 9 May 2023 doi:10.20944/preprints202305.0597.v1

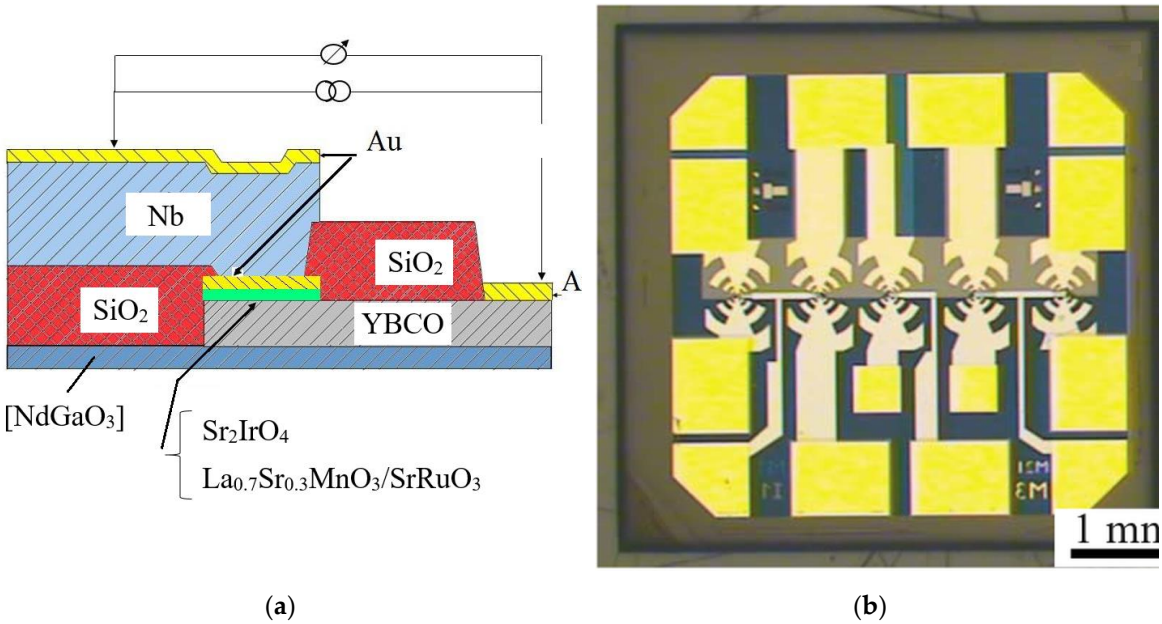

(**a**) (**b**)

Figure 1. (a) Cross-section of the MS with thickness of layers: $YBa_2Cu_3O_{7-x}$ d_{YBCO} =60–70 nm, Sr_2IrO_4 film d_{SIO} = 5–7 nm, $La_{0.7}Sr_{0.3}MnO_3$ d_{LSMO} =3 –15 nm, Sr_2IrO_4 d_{SRO} =4 – 10 nm. **(b)** Photo from top of substrate with 5 MSs. Adopted from [59,65].

A protective Au thin film with thickness about 10 nm was deposited *in situ* at 30 °C in the PLD chamber. The superconducting top electrode Nb film with thickness about 200 nm was deposited *ex situ* by magnetron sputtering in argon atmosphere at room temperature, followed after the pre-sputtering of Au film [65]. Nb/Au/B/YBCO mesa-structures (MS) illustrated in Figure 1a had square shape and side sizes from L = 10 μm to 50 μm. Total five MS on a chip (see Figure 1b) were formed using optical lithography, reactive ion-plasma etching, and ion-beam etching at low ion accelerating voltages. Oxygen plasma treatments were performed after each lithography process to remove the remains of the resist. The SiO_2 protective insulator layer was deposited by rf sputtering provided the DC current to flow in perpendicular direction to the B interlayer. An additional Nb film with a thickness of 200 nm was sputtered providing superconducting current transport through the DC wiring. Contact pads were made of gold films for four-point *I-V* curve measurements, schematically shown in Figure 1a. A chip with 5 MS with either composite interlayer LSMO/SRO – C-MS, or SIO film interlayer – S-MS is shown in Figure 1b. Thicknesses of interlayer films varied in the range 2–50 nm [31–36,60,61].

3. Results

3.1. DC transport characteristics

The results of experimental investigations of the hybrid heterostructures (M-MSs) of the Nb/Au/M/YBCO type, where M is a magnetically active material are presented in Figure2. In order to conclude whether a single magnetically active film used as a interlayer leads to superconducting current several magnetically active films were examined: the undoped $LaMnO_3$ (LMO) manganite, as well the optimally doped compositions $La_{0.7}Ca_{0.3}MnO_3$ (LCMO), and the LSMO. The optimum doping level implies an impurity concentration corresponding to the maximum of Curie temperature. The data of resistance measurements were compared with the results of calculations using quasi-classical equations of the theory of superconducting weak links [22].

Preprints (www.preprints.org) | NOT PEER-REVIEWED | Posted: 9 May 2023 doi:10.20944/preprints202305.0597.v1

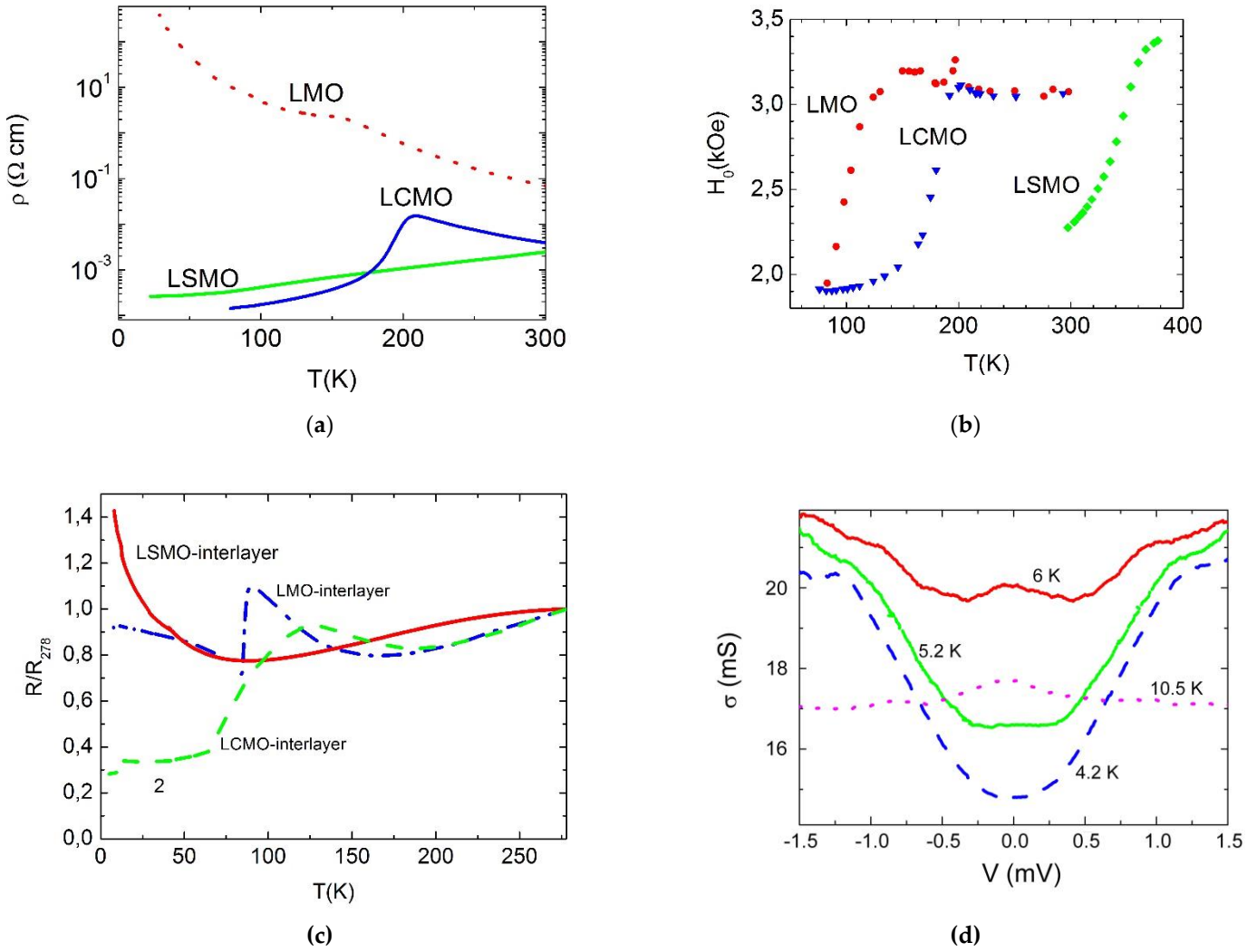

Figure 2. (a) Temperature dependences of resistivity of the single manganite films deposited directly onto substrate. **(b)** Temperature dependences of ferromagnetic resonance field H_0, measured at F= 9.76 GHz for manganite films: red point LMO; blue triangular - LCMO; green square - LSMO. The Curie temperature T_{CU} was determined at the point of transition from a weak growth (characteristic of a paramagnetic phase) to a sharp drop in $H_0(T)$: T_{CU}(LMO) = 150 K; T_{CU}(LCMO) = 200 K; T_{CU}(LSMO) = 370 K. **(c)** Temperature dependences of the normalized $R(T)/R(T$=278 K) resistance of M-MS with manganite interlayers: blue dash–dot LMO; green dashes LCMO; red solid line LSMO. Local maxima correspond to metal-insulator transition. **(d)** A family of plots of the conductivity σ vs. voltage V for M-MS with LCMO interlayer measured at various temperatures within T=4.2 - 10.5 K interval. Adopted from [22].

Manganite M interlayer materials were studied for their temperature dependences of resistivity $\rho(T)$. Obtained results for LMO, LCMO and LSMO are shown in Figure 2a. A transition in $\rho(T)$ function at temperature T_{MI} usually takes place not far from the Curie temperature T_{CU} of magnetic film. As seen from Figure 2a the well pronounced metal-insulator transition for LCMO film occurs at T = 210 K. At higher temperatures T>T_{CU} the $\rho(T)$ behavior takes form of a thermally activated type, while at the lower temperatures T< 210 K it is rather a metallic-like. For Sr-doped manganite LSMO film the Curie temperature T_{CU} is of order of 350 K and at T > 300 K and is not seen in Figure 2a. In the undoped manganite LMO the metal–insulator transition was not observed clearly enough, just a weak singularity is seen as a change in curvature of $\rho(T)$ function. A significant rise of the LMO film

Preprints (www.preprints.org) | NOT PEER-REVIEWED | Posted: 9 May 2023 doi:10.20944/preprints202305.0597.v1

resistivity by several orders in magnitude at low temperatures distinguishes the LMO from doped manganites LCMO and LSMO.

Using measurements of ferromagnetic resonance (FMR) changing the ambient temperature the Curie temperature of manganite films could be determined. Temperature dependences of FMR magnetic field H_0 were measured frequency F= 9.76 GHz. Figure 2b demonstrates the evolution of FMR field H_0 with temperature decrease for all three type of manganites, and a sharp drop in $H_0(T)$ functions took place at temperatures approaching T_{CU}. A weak increase on $H_0(T)$ dependences at somewhat higher temperatures relative the T_{CU} is seen well for LMO and LCMO films being explained by their temperature behavior of paramagnetic phase. As Curie temperature of LSMO is near 350 K its $H_0(T)$ dependence is shifted toward high temperatures. Obtained data for T_{CU} values somewhat differ from those determined from susceptibility measurements of single crystalline manganites which are strongly dependent on the quality of crystalline films, strain, and the stoichiometry with respect to the oxygen content [66]. The T_{CU} value for the undoped LMO was near 100 K. An appearance of ferromagnetism in the doped manganites (LSMO and LCMO) is described by the double exchange between Mn3+ and Mn4+ ions [67], while in manganites with low levels of doping the antiferromagnetic phase may occur due to super-exchange between Mn3+ ions. An important role in such interactions of Mn3+ and Mn4+ ions is played by the Jahn–Teller distortion [68,69]. Thus, the ferromagnetic phase exists even in the undoped stoichiometric antiferromagnetic LMO as well in the case of nonstoichiometric $LaMnO_{3+\delta}$. The strain in the thin film caused by the crystalline mismatch with the substrate [66] in LMO enhances the ferromagnetism analogously to the case of external pressure [69]. Figure 2c shows dependences of normalized (by $R_{278} = R(T=278\ K)$ resistance R/R_{278} vs. temperature for M-MS structures with all three types of manganite interlayers. At relatively high temperatures (T>150 K), the $R/R_{278}(T)$ dependences are determined first of all by the contribution of the resistivity of YBCO electrode, which $R(T)$ dependence lays at relatively high resistance range. A small deviation from the linear $R(T)$ behavior for M-MS with LSMO interlayer is related to it's high Curie temperatures T_{CU} > 300 K. A decrease in resistivity at $T \leq T_{CU}$ is caused by impact resistivity of YBCO film which has transition temperature to the superconducting state at temperatures T≈80 K. A sharp drop of $R(T)$ functions occurs at the temperature below superconducting transition $T \leq T_C$ (amount 8.5 K) of Nb/Au electrode. Note, the superconducting transition of the Nb/Au electrode for the M-MS structures with LSMO interlayers demonstrates too weak change of $R(T)$ function at low temperatures and was not observed. It is also seen that the contributions of resistances from the manganite M-interlayers and from superconductor/manganite interfaces are strongly manifested at the temperatures near the metal–insulator transition T_{MI}, which is close to the Curie temperature T_{CU}. In this case, the $R(T)$ function and parameters T_{MI} and T_{CU} depend on the composition (stoichiometry and doping) of manganite interlayer. For M-MS with LSMO interlayer with high T_{CU} values, the interlayer resistance, as well the resistance of S_d electrode YBCO film contributed to the $R(T)$ at temperatures above superconducting transition $T>T_C$. At low temperatures the M-MS structures with LSMO and LMO (in contrast to LCMO) M- interlayers exhibit an increase of resistance in $R(T)$ with temperature lowering. The resistivity at T = 4.2 K of LCMO M-film deposited directly onto the substrate and amounted $\rho_M=10^{-3}$ Ωcm contributes to resistivity of M-MS, characterized by value $R_MS = \rho_M d_M = 10^{-9}$ Ωcm² for the case of M-film thickness d_M =10 nm. Note, the characteristic resistance of M-MS with LCMO thickness d_M = 10 nm was $R_NS \approx 2\ 10^{-4}$ Ω cm² is much greater in experiment than the calculated one. Thus, we can conclude that the resistance of M-MS with the LCMO M-interlayer at low temperatures is determined mainly by the resistances of barriers I_1 and I_2 which originate between the interlayer and the adjacent superconducting film in M-MS, while the resistance of M-interlayer is relatively small and can be ignored. Taking into account the interface Au/M resistance, determined from additional measurements [70] and the total resistance of M/S_d structure it turns out that the S/M interface (here S is Nb/Au is superconducting bilayer as the mean free path of Au l ~ 100 nm is much thinner that Au film thickness d_{Au}) has low transparency. Thus, the M-MS heterostructures could be modeled as $S/I_1/M/I_2/S_d$, in which the barriers I_1 and I_2 are the S/M and M/S_d interfaces, respectively. The superconducting S-electrode of Nb/Au bilayer is an ordinary superconductor with the s-wave symmetry of the order parameter, while the S_d electrode made of cuprate YBCO superconductor has a predominantly d-wave symmetry of order parameter

Preprints (www.preprints.org) | NOT PEER-REVIEWED | Posted: 9 May 2023 doi:10.20944/preprints202305.0597.v1

pair potential. An example of conductivity temperature dependence $\sigma(V)$ functions for M-MS with the d_M = 10 nm thick LCMO interlayer are shown in Figure 2d, measured at 4 fixed temperatures. It is seen that conductivity decreases at low voltages and exhibits bending-like behavior around the voltage of superconducting eergy gap of Nb film. Superconducting correlations penetrate from the Nb/Au S-superconductor into the interlayer and modify the density of states. Importantly, no superconducting current exist in heterostructures with any of single manganite LMO, LCMO, or LSMO interlayer. Experimentally this was proved also by measurements reducing temperature well enough below temperature of liquid helium T < 4.2 K [22] down to T=0.3 K [71] and reducing also the interlayer thicknesses to d_M = 5 nm. Note, an occasionally appearance of a superconducting critical current at small values of the M-interlayer thickness (d_M < 5 nm) was proved is related to pinholes appearing in the structure [32]. Particularly, our measurements showed that pinholes lead to the absence of oscillatory dependences of the critical current and Shapiro step amplitudes vs. power of external microwave electromagnetic field. In MS S/S_d structures (Nb/Au/YBCO junctions) without additional interlayer [65] exhibited well pronounced superconducting current and Josephson effect, attributed to the spin-singlet pairing. The absence of superconducting current in M-MS is explained by very weak superconducting proximity effect at S_d/M interface of penetration of superconducting correlations with d-wave symmetry of YBCO S_d film to the manganite M-interlayer, or, more precisely, by the negligibly small value of the *s*-wave component, which also exists in YBCO and penetrates into the M interlayer into a depth equal to the electron mean free path l, small compared to the interlayer thickness d_M [72]. Spin-singlet superconducting correlations in S/F/S structures are well known [73] when exchange interaction in ferromagnetic F interlayer does not prevent superconducting transport and observation Josephson effect, enabling to prepare so-called π-junctions [74]. The case of S/AF/S junctions with an antiferromagnetic AF-interlayer are less studied. In this connection it should be noted that the stoichiometric LMO is antiferromagnetic, however, a small deviation from stoichiometry of LMO thin film may lead to a weak ferromagnetism. This behavior is analogous to that observed for the M-MS with the LCMO M-interlayer.

The C-MS demonstrated rather different behavior. The temperature dependence of resistance $R(T)$ of a typical C-MS (see Figure 3a) contains two parts, the both show decrease of resistance with cooling from room temperature down to T=4.2 K. Resistance drops correspond to transition to the superconducting state of S_d (YBCO) film and S (Au/Nb)film. Above the superconducting transition temperature for YBCO $T \geq T_C$ (YBCO) the $R(T)$ dependence exhibits a typical for the superconducting cuprate a metal type linear behavior. At temperatures $T \leq T_C$ (Nb) below transition temperature Au/Nb electrode the C-MSs demonstrated superconducting critical current I_C temperature dependence $I_C(T)$ as shown in Figure 3b.

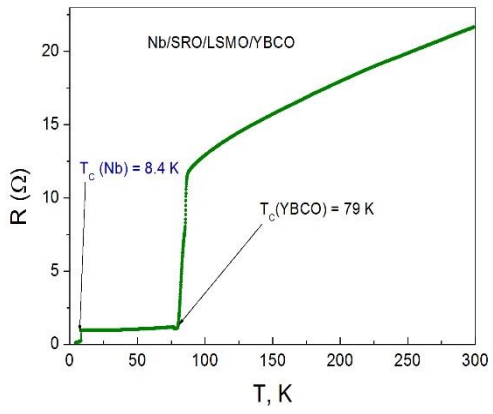

(**a**)

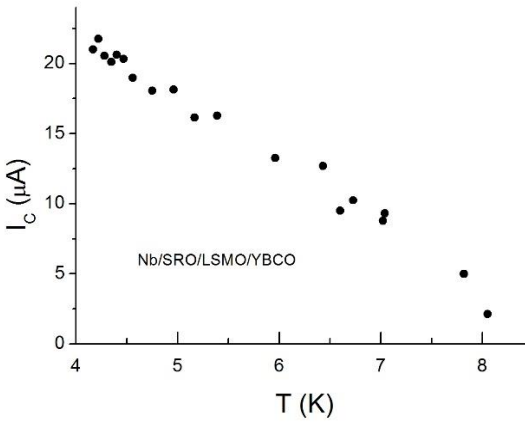

(**b**)

Preprints (www.preprints.org) | NOT PEER-REVIEWED | Posted: 9 May 2023 doi:10.20944/preprints202305.0597.v1

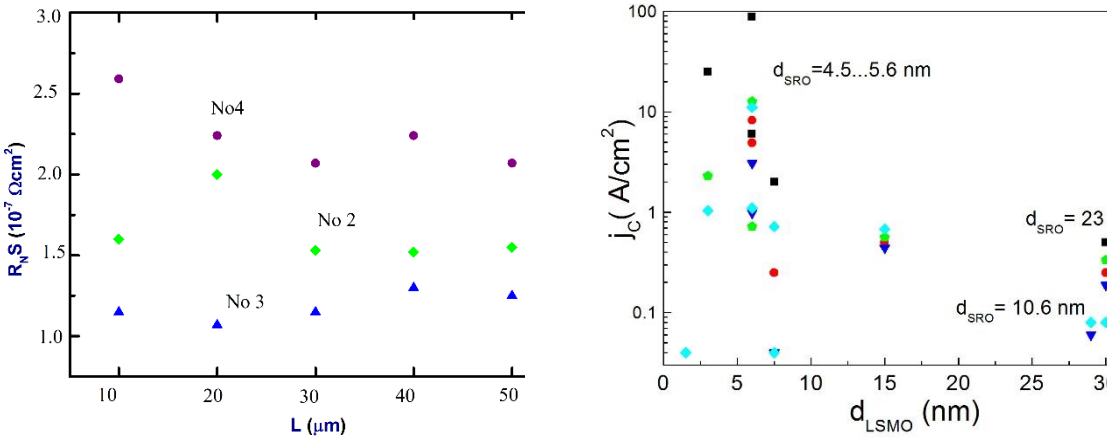

(c) (d)

Figure 3. C-MS: **(a)** Temperature dependence of $R(T)$ C-MS for L=10 μm, d_{LSMO}=3 nm d_{SRO}=5.5 nm, **(b)** Temperature dependence of critical current $I_C(T)$. **(c)** Size-L dependence of characteristic resistance R_NS for 15 C-MS indicating reproducibility of the samples. **(d)** Critical current density j_c dependence on d_{LSMO} for fixed d_{SRO}=4.5-23 nm. Adopted from [31,34].

The parameters of critical current densities $j_C=I_C/S$, $S=L^2$ for several C-MSs with the composite interlayer LSMO/SRO are given in Table 1. An important parameter for Josephson junctions and for C-MS as well is the specific resistance R_NS, where R_N is the normal state resistance, is also presented in Table 1. Figure 3c shows the values of characteristic resistance R_NS for 3 chips of C-MS obtained for all 5 mesa-structures with different size L. It can be seen that the values of R_NS differ from chip to chip, but remain almost the same within a chip, having the same thickness of the LSMO and SRO films in the B-interlayer. In comparison with R_NS values of YBCO/Au/Nb structures without B-interlayer [65] an insertion of composite LSMO/SRO interlayer results in significant decrease of R_NS. To compare the resistive characteristics of the interfaces in mesa-structures with different interfaces we additionally prepared structures with a single ferromagnetic interlayer [34]. The value of R_NS for structures with the SRO interlayer is almost three orders in magnitude smaller than for the structure with the LSMO interlayer [34]. Assuming that the specific resistance of the LSMO/Au interface does not exceed 1 μΩ cm² [34], the high R_NS values of the YBCO/LSMO/Au structures (R_NS ~ 100 μΩ cm²) can be explained by the high resistance of the YBSO/LSMO interface. Thus, the transparencies of interfaces in C-MS: YBSO/SRO, SIO/LSMO and LSMO/Au are high enough and allow superconducting current to flow.

Superconducting critical current was observed for the C-MS with the total thickness of the composite interlayer up to 50 nm (see Table 1). Importantly, there were no superconducting current in structures with a single ferromagnetic interlayer (LSMO or SRO) with a thickness exceeding 5 nm, which is equal in order of magnitude to the coherence length ξ_F in magnetic film. Figure 3d demonstrates j_C dependence vs. thickness of LSMO film for 3 thicknesses of SRO in composite B-interlayer in C-MS. The existence of the critical current and its the power-low decrease for composite interlayer exceeding thickness of 5 nm indicate the transport of spin-triplet superconducting correlations through the thick ferromagnetic interlayer [24,32]. However, a spread in the values of the critical current densities for different chips and within a chip noticeably exceeded the spread in the values of R_NS.

Preprints (www.preprints.org) | NOT PEER-REVIEWED | Posted: 9 May 2023 doi:10.20944/preprints202305.0597.v1

Table 1. DC parameters of C-MS.

Number	d_{SRO}, nm	d_{LSMO}, nm	L, μm	R_NS, μΩcm²	j_C A/cm²
1	14	0	20	0.11	0
2	0	2	20	120	0
3	4.5	3	50	0.45	0.75
4	8.5	3	10	0.13	25
5	8.5	6	10	0.16	88
6	5.6	15	50	0.20	1.1
7	10	9	30	0.15	2.2

d_{SRO} and d_{LSMO} are the thicknesses of the SRO and LSMO films correspondingly; L is the linear size of the C-MS, jc is the critical current density, R_N is the normal resistance, and $S = L^2$ is the C-MS area.

Let us now to estimate the coherence length in the films forming the interlayer in C-MS. Since the electron mean free path l in oxide materials (SRO and LSMO) is quite small [75,76], we can assume that the electron transport is of a diffusion type exhibiting scattering from the SRO/LSMO interface due to the difference in the Fermi velocities. In the case of diffusion, the coherence length in a normal nonmagnetic material is $\xi_N = (\hbar D/T)^{1/2}$, while its value in a ferromagnetic material is $\xi_F = (\hbar D/Eex)^{1/2}$, where $D = v_F l/3$ is the diffusion coefficient and v_F is the Fermi velocity. We can estimate the mean free path l using the semi-empirical relation $l = l_{ph}(R_{300\,K}/R_{4.2\,K} - 1)$, where l_{ph} is the phonon mean free path (about 0.4 nm for LSMO and 1 nm for SRO [76]). The measured $R(T)$ dependences show that $R_{300\,K}/R_{4.2\,K} \approx 3$ for SRO films grown on the (110)NGO substrate and $R_{300\,K}/R_{4.2\,K} \approx 10$ for LSMO films grown on (110)NGO substrate. This gives $\xi_F \approx 8$ nm for LSMO and $\xi_F \approx 3$ nm for SRO, respectively, both smaller than the thickness of the interlayer in C-MS.

Changing the interlayer from the composite SRO/LSMO one to a material with SOI also allowed to observe superconducting current in Nb/Sr_2IrO_4/YBCO mesa-structures (S-MS). The I-V curve and the differential resistance dependencies $R_D(I) = dV/dI$ at T=4.2 K are presented on Figure 4a. The dependences of $R_D(V)$ in larger scale at two temperatures: at T=4.2 K, and at $T>T_C$ of Nb are shown in Figure 4b. Singularities on $R_D(V)$ functions at the bias voltages equal to the voltage of Nb energy gap $V=V_\Delta$ are seen very well. The variation of the central part of $R_D(V)$ with a dip caused by zero-bias conductance peak on the curve taken at $T>T_C$ is shown in Figure 4d. After deposition of the superconducting top electrode Nb film and wiring pattering, the transition temperature of the YBCO in the S-MS reduced to $T_C \approx 61$ K, affected by influence of ion-beam etching and oxygen migration at SIO/YBCO interface. The normal state resistivity of Nb/Au interface, studied earlier [65], gave $R_NS = 10^{-6}$ μΩcm², corresponding to a transparency $\Gamma \approx 1$ which does not reduce the transparency of $\Gamma = 10^{-2}$-10^{-3} [34].

Preprints (www.preprints.org) | NOT PEER-REVIEWED | Posted: 9 May 2023 doi:10.20944/preprints202305.0597.v1

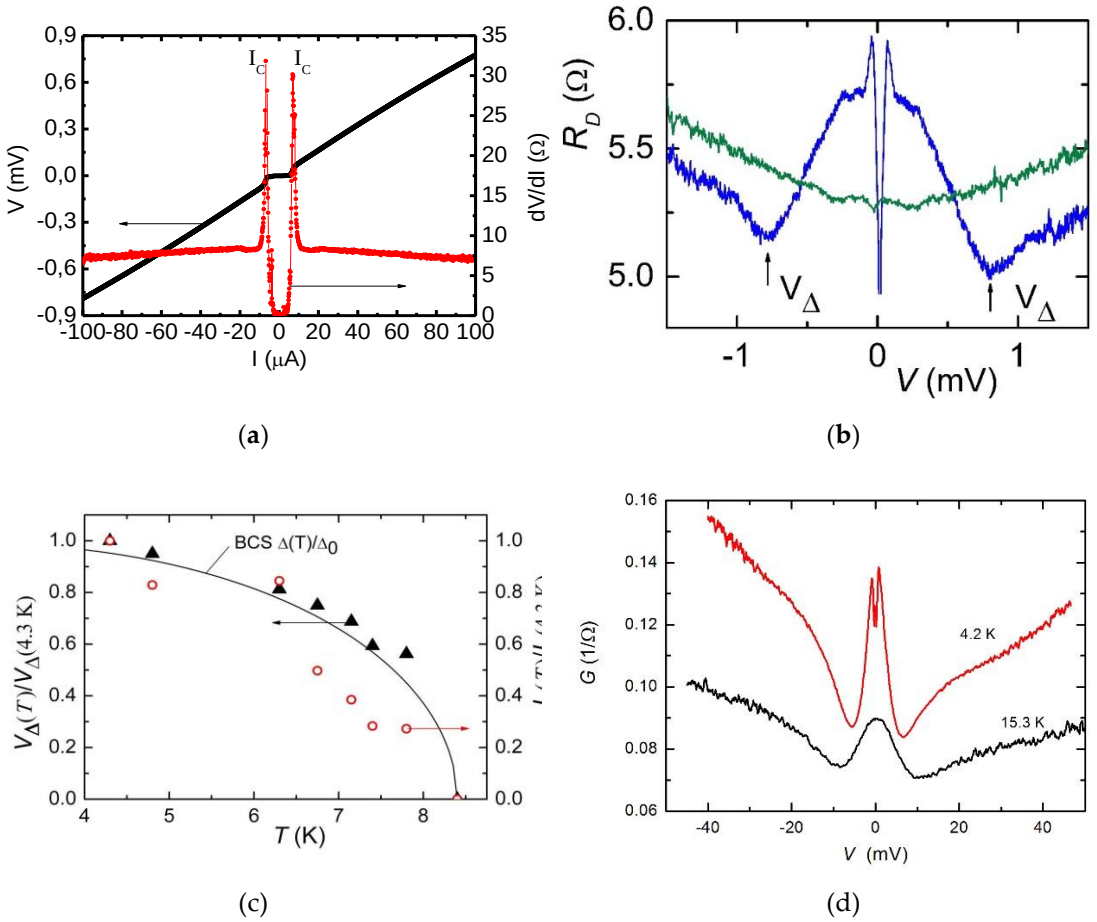

Figure 4. S-MS d = 7 nm: **(a)** I-V curve and current dependence of differential resistance dV/dI(I). The critical current I_C is determined by the local maxima of dV/dI. **(b)** Singularities on R_D =dV/dI (V) caused by the energy gap of the Nb electrode shown by arrow at T = 4.2 and 8.4 K. **(c)** Temperature dependences of the normalized critical current I_C and gap voltage V_Δ. A solid line is the BCS dependence of the energy gap vs. temperature. **(d)** Voltage dependence of conductivity G(V) for S-MS with L = 40μm at temperatures T = 4.2 and T=15.3 K. Adopted from [64].

Table 2 presents DC parameters of S-MS with d_{SIO}=7 nm. The averaged values of specific resistivity R_NS for 4 S-MS located on one chip with the same SIO thickness d_{SIO} = 7 nm was estimated $R_NS \approx 100$ μΩcm² at temperature T = 4.2 K. Note, an expected contribution to the total resistivity from SIO film calculated, taking experimental value $\rho d_{SIO} = 7\ 10^3$ μΩcm², should be much higher [64]. This explains the difference in measured value of R_NS from a simplified prediction and allows to argue that the tunneling is the main mechanism of electrical transport through the SIO/Au interfaces in the S-MS. Low transparency $\Gamma = 3\ 10^{-5}$ of SIO/Au interface is also inherent to tunnel-like junctions. At the same time there exists a drop of resistivity around the biasing voltage V=0. The appearance of zero-bias conductance peak (ZBCP) was observed as shown in Figure 4d. This demonstrates that the SIO/YBCO interface is a transparent enough and it points on occurrence of low-energy states enabling coherent electron transport over them. Thus, for a model of S-MS structure the SIO/YBCO interface could be considered as N_{SO}/S junction, where N_{SO} is a normal metal with SOI, and S is a singlet superconductor. The parameters of S-MS (normal state resistance R_N, and critical current I_C) could be extracted from I-V characteristics measured at d.c. (see Figure 4a). For junction characterization experimental dependences of differential resistance R_D = dV/dI from biasing current I are also useful. At temperatures near superconducting transition temperature T_C of Nb film the critical current

Preprints (www.preprints.org) | NOT PEER-REVIEWED | Posted: 9 May 2023 doi:10.20944/preprints202305.0597.v1

amplitudes I_C were small and in order to determine the critical current values the $R_D(I)$ functions were used as described in [64], since the influence of low frequency fluctuations resulted in "rounded" *I-V* curves.

The experimental $I_C(T)$ function and the temperature dependence of the voltage at which the energy gap singularity V_Δ on $R_D(V)$ takes place, caused by Nb electrode, the $V_\Delta(T)$ dependence was obtained and it is shown in Figure 4c along with the normalized theoretical BCS temperature dependence of Nb energy gap. Taking into account the conductance $G(V)$ rise at voltages V>10 mV, observed at low temperatures, the S-MS could be modeled as S/I/N_{SO}/S_d junction. The rise of conductivity at voltages $V >> V_\Delta$ is inherent to tunneling type of electron transport and for S-MS could be caused by existence of an insulating barrier I between SIO and Au/Nb superconducting S bilayer.

Table 2. DC parameters of S-MS with thickness of SIO interlayer d_{SIO}=7 nm.

Number	*L*, μm	R_NS, μΩcm²	j_C, A/cm²	I_CR_N, *μV*	λ_J, *μm*
1	*50*	*125*	0.75	*32*	*725*
2	*40*	*114*	25	*43*	*600*
3	*30*	*94*	88	*31*	*645*
4	*20*	*83*	13	*10*	*1065*

L is the linear size of mesa-structures, *jc* is the critical current density, R_N is the normal resistance, and $S = L^2$ is the mesa-structure area.

3.2. Magnetic field dependences.

Figure 5 show magnetic moment $M(H)$ for Au/LSMO/SRO/YBCO heterostructure for in-plane and normal-to-plane directions of *H*-field at different temperatures. Measured by SQUID magnetometer the magnetization of LSMO film lies in the plane of the substrate, whereas the magnetization vector of the SRO film was directed at an angle of about 23° from the normal to the plane of the substrate. The LSMO is characterized by a coercive force of 20–30 mT and exchange energy of 2.3 meV [77] while the SRO has coercive force of the order of 1 T and an exchange energy of 13 meV [78].

Note, in order to turn the vector of the SRO magnetization and to make it collinear to the direction of LSMO magnetization, one needs to apply in-plane magnetic field of order 1 T [32]. So, this apparently confirms magnetic nature of the both SRO and LSMO films in the interlayer of C-MS. At these circumstances no superconducting current should be observe for the case of singlet pairing of superconducting correlations.

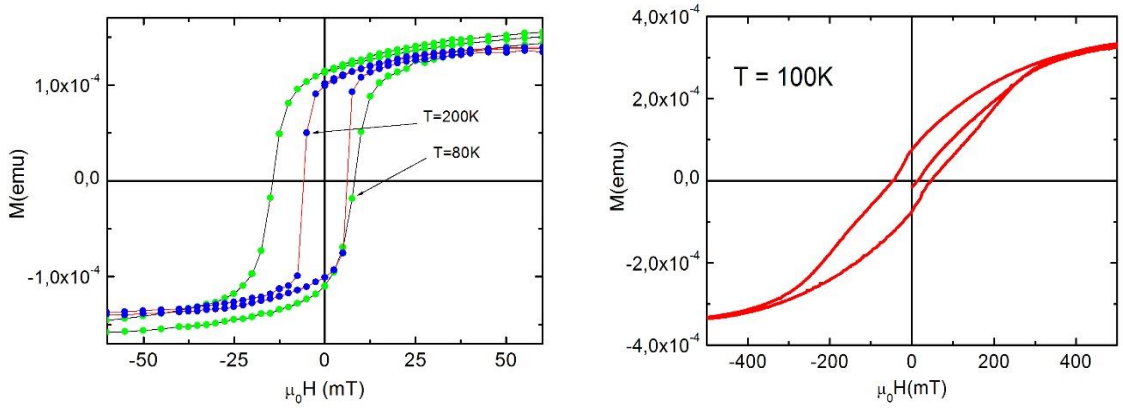

(**a**) (**b**)

Figure 5. (a) Magnetic field dependence of the in-plane magnetic moment at the two temperatures at *T*=80 K and *T*=200 K for Au/LSMO/SRO/YBCO/LAO heterostructure. **(b)** The same dependence at *T* = 100 K for magnetic field applied normal to the substrate surface. Adopted from [32].

Preprints (www.preprints.org) | NOT PEER-REVIEWED | Posted: 9 May 2023 doi:10.20944/preprints202305.0597.v1

For the Josephson junction with superconducting current-phase relation $I_S=I_C\cdot\sin\varphi$ and uniform distribution of superconducting current density, the magnetic field dependence of critical current $I_C(H)$ is described by the *sinc*-function as the Fraunhofer diffraction pattern [79]. When the external field H through the cross-section $S_J= Ld_J$, the magnetic permeability of the layers must be taken into account $d_J= \mu_1 d_{LSMO}+\mu_2 d_{SRO}+\lambda_{Nb} +\lambda_{YBCO}$ where λ_{Nb} = 90 nm and λ_{YBCO} = 150 nm are the London penetration depths of the magnetic field for Nb and YBCO, respectively, and $\mu_{1,2}$ is the magnetic permeability of LSMO and SRO films, the Josephson junction produces flux $\Phi=\mu_0 HS_J$ equal to magnetic flux quantum Φ_0 =h/2e≈2.068×10^{-15} Wb then $I_C(H)$ demonstrates zeros. In experiment the measured magnetic field dependences of $I_C(H)$ of S-MS were markedly different from Fraunhofer pattern (see Figure 6a). This could be explained by difference of CPR from $\sin\varphi$, as reported for Josephson junctions with spin-triplet component. In this regard the magnetic field dependences are important. Moreover, the critical current was observed at considerably high levels of magnetic field up to 0.2 T (see Figure 6a).

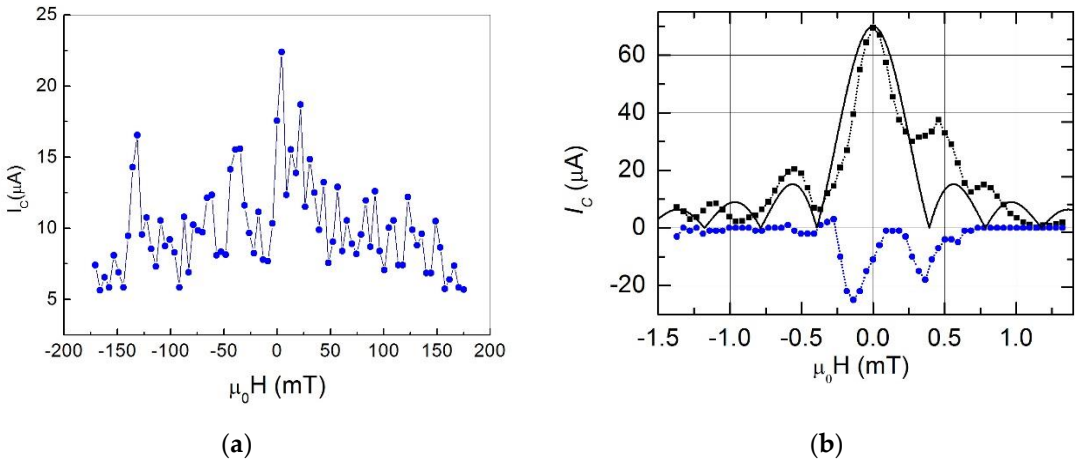

Figure 6. (a) Magnetic field dependence of critical current for C-MS. **(b)** Magnetic field dependence of critical current of S-MS for two direction of current biasing. An asymmetry of I_C is clearly observed. Adopted from [34,80,81].

A dependence $I_C(H)$ of superconducting critical current vs. magnetic field H for S-MS with SIO thickness d_{SIO}=5 nm, L=40 μm is shown in Figure 6b. Magnetic field H was applied in parallel, using multi-turn thin amorphous mu-metal shield which reduces geomagnetic field about 10 times. It is seen that the maximum of total value of I_C is located at H=0 and the shape of $I_C(H)$ deviates from the ordinary dependence of usual Josephson junction. There exists an asymmetry of $I_C(H)$ function relative the direction of applied magnetic field change (see Figure 6b). Positive I_{C+} and negative I_{C-} critical current amplitudes are different, shown by a separate curve. Such a "large" Josephson junction behavior usually happens when junction size L exceeds the Josephson penetration depth λ_J at least over 2 times, $L>2\lambda_J$ [79]. In our experimental case, on contrary, the S-MS is 4 times shorter L than Josephson penetration depth, which is estimated as λ_J =170 μm. The difference $\Delta I_C=I_{C+}+I_{C-}$ and the I_C amplitude defined at V=0, $I_C=(I_{C+} - I_{C-})/2$ are given in Figure 6b. Theoretical Fraunhofer pattern $I_C(H)$ dependence is also given. The calculated level of magnetic field H_1 at the first minimum of $I_C(H)$ Fraunhofer dependence could be fitted for discussed S-MS sample, using estimated value of $H_1=\Phi_0/\mu_0 d_J L\approx 4$ Oe, where $d_J=d+\lambda_{Nb}\mathrm{ctanh}(d_{Nb}/2\lambda_{Nb})+\lambda_{YBCO}\mathrm{ctanh}(d_{YBCO}/2\lambda_{YBCO})$, taking magnetic field London penetration depths for YBCO and Nb at T=4.2 K λ_{YBCO}=150 nm, λ_{Nb} = 90 nm, correspondingly. Note, for S-MS with d_{SIO}=7 nm [64] with small superconducting current density j_S and, as result, small critical current I_C amplitude, the difference between positive I_{C+} and negative I_{C-} critical currents amplitudes hardly could be identified experimentally. However, a difference between positive I_{C+} and negative I_{C-} critical currents may point on anomalous Josephson effect with phase shift in CPR.

Preprints (www.preprints.org) | NOT PEER-REVIEWED | Posted: 9 May 2023 doi:10.20944/preprints202305.0597.v1

Such behavior requires to meet specific conditions [82], for example, it happens in structures with splitting in spin bands due to influence of SOI [81,83]. Note, in our experiment conditions the level of applied magnetic field H was much smaller than that, required for Zeeman splitting. At the same time another interesting feature (will be discussed below) has been revealed in our experiment, which hints on possible influence of magnon-plasma wave interaction [84,85].

3.3. Microwave characteristics

The analysis of high frequency dynamics of critical current amplitudes and Shapiro steps taking place on the I–V curves under the action of applied microwave radiation indicates the lack of direct contacts (pinholes) between superconductors. The oscillations of Shapiro steps depending on the microwave power were observed and the amplitudes of these oscillations conformed well with the modified resistively shunted Josephson junction (MRSJ) model [65].

The amplitude of Josephson self-oscillations I_J is enhanced with biasing voltage V and frequency, obeying relation $f_J=(2e/h)V$. There exist a several limits for I_J rise with frequency f_J, e.g. superconducting energy gap, heating, and so on. At frequencies f_J approaching the critical frequency $f_C=(2e/h)I_CR_N$ function $I_J(f_J)$ saturates in accordance of resistively shunted junction (RSJ) model [79]. The parameter f_C of Josephson junction could be evaluated from I-V characteristics measured at d.c., but characterization at microwave frequencies remains important, particularly for our MS. In the case of C-MS with a relatively low f_C the microwave studies were carried out in very wide frequency band. We registered Shapiro steps on the I-V characteristics registered at frequency of external signal $f_e>>f_C$ at relatively low frequency f_e=80 MHz for C-MS with I_C=27.5 μA, R_N=8 mΩ at T=4.2 K when external RF signal was weakly coupled with junction through air [36]. In spite of large impedance mismatch an occasional high-Q resonant coupling leads to good enough transmission of electromagnetic radiation from the open-ended coaxial output to the wiring leads. In the case of resonant coupling using additional print-on filters at desired frequency bands the impact of external noise is reduced.

Figure 7a demonstrated a family of I-V curves with Shapiro steps, registered at different levels of applied power of microwave signal at frequency f_e=41 GHz which is about 500 times higher frequency than 80 MHz. Figure 7b shows the first (n=1) Shapiro step marked I_1, and half-integer steps (n=1/2) for C-MS with parameters L= 10 μm, I_C = 88 μA, and R_N = 0.16 Ω. The maximum of the first Shapiro step was I_1 = 94 μA and, correspondingly, the ratio I_1/I_C = 1.1 is in well agreement with the RSJ model. A deviation of the CPR from sinusoidal $I_S(\varphi)=I_C\cdot\sin\varphi$, was obtained by measurements of critical current dependencies from magnetic field $I_C(H)$ [30].

In C-MS the s-wave Nb/Au superconducting S-electrode contacts the YBCO S_d -electrode via the Sr_2IrO_4 interlayer. The order parameter of YBCO superconductor could be described as a superposition of d-wave (Δ_d) and s-wave (Δ_s) components, in which $\Delta(\theta)=\Delta_d\cos2\theta+\Delta_s$, where θ is the angle between the quasiparticle momentum and the a-axis of the YBCO crystal structure. In the case of S/S_d junction between Nb/Au bilayer and the YBCO film, the CPR differs from the sinusoidal, particularly for the case of electron transport along the c-direction of the YBCO S_d film [65,86–88]:

$$I_s(\varphi)=I_{c1}\sin\varphi+I_{c2}\sin2\varphi \quad (1),$$

where the amplitudes I_{c1} and I_{c2} are the critical currents for the first and the second harmonics in CPR. The ratio $q=I_{c2}/I_{c1}$ is used as a characteristic parameter for the second harmonic weight. The d-wave component order parameter (Δ_d) in YBCO superconducting electrode leads to unconventional superconducting CPR of the junction with the nonzero 2nd harmonic amplitude [65]. From calculations in [65] we learned that at small $q\leq0.5$ the difference between I_{c1} and the total I_C is smaller than 20% and increases with q starting from $q>0.5$ [89]. The first harmonic I_{c1} may originate from the minor s-wave component also existing in YBCO (Δ_s), and if $\Delta_d>>\Delta_s,\Delta_{Nb}$ the I_CR_N product for the case of a dominated 1st harmonic looks [65]:

$$I_{c1}R_N\approx\Delta_s\Delta_{Nb}/(e\Delta_D^*) \quad (2),$$

Preprints (www.preprints.org) | NOT PEER-REVIEWED | Posted: 9 May 2023 doi:10.20944/preprints202305.0597.v1

where e is electron charge, $\Delta_D^*=\pi\Delta_d[2\ln(3.56\Delta_d/k_BT_{cNb})]^{-1}$, k_B is Boltzmann constant. For MS with $V_\Delta(4.2\ K)\approx 0.8$ mV the parameters $\Delta_{Nb}/e\approx\Delta_s/e$ are also 0.8 mV and taking a typical estimate for $\Delta_d/e\approx 20$ mV we get $I_{c1}R_N\approx 60$ μV calculated by (2). It is twice larger than the experimentally obtained values of I_CR_N (see Table I), and close to the case of a S/S_d junction without interlayer in which the S_d electrode is contacting to s-wave S electrode in direction of YBCO c-axis [65]. Thus, inserting the Sr_2IrO_4 interlayer between YBCO and Au/Nb results in a reduction of $I_{c1}R_N$ product.

Note again, no superconducting current was registered in mesas with the ferromagnetic interlayers using 3d manganite materials $La_{0.7}Sr_{0.3}MnO_3$, $La_{0.7}Ca_{0.3}MnO_3$ or $LaMnO_3$ [90]. Thus, specific properties of Sr_2IrO_4 which is 5d material with strong SOI should be taken into account [91]. Oxygen migration at Sr_2IrO_4/YBCO interface could play the decisive role for appearance of superconducting current in S-MS through the thick Sr_2IrO_4 interlayer (in comparison with the coherence length). According to experimental data [89] even a minor change in the oxygen content in Sr_2IrO_4 leads to a drastic change in the conductivity type of Sr_2IrO_4 at low temperature from activation to metallic.

As it was already shown in Figure 4d a difference of conductivity $G(V)$ and the existence of ZBCP is well seen at T= 15.3 K, at the same time we'd like to note that evolution of conductivity $G(V)$ started from higher temperatures, at least from T=48 K [64]. Existence of ZBCP in experimental data shows that the Sr_2IrO_4/YBCO interface is quite transparent and low energy states predicted for d-wave superconductor and Sr_2IrO_4 [45,63] could be relevant. When the SOI is taken into account at the Sr_2IrO_4/YBCO interface [92] a spin-triplet component of superconducting current occurs along with the long range proximity effect [44,45] and taking into account the oxygen changing at the adjacent part of Sr_2IrO_4 the latter becomes well conducting and theoretical models [8,9,44,45] for spin-triplet superconducting current in junctions with spin-singlet superconductors coupled by a normal metal with SOI could be applied.

Assuming presence of second harmonic, CPR takes form $I_S(\varphi)=I_{C1}\cdot\sin\varphi+I_{C2}\cdot\sin 2\varphi$ characterized by ratio $q=I_{C2}/I_{C1}$, which could be estimated by measurements of Shapiro steps heights vs. $a=I_{RF}/I_C$ of applied microwave current I_{RF} and utilizing the model [65] which takes into account the impact of both the junction capacitance C and q. At high frequency limit $\omega=f_e/f_C>1$ and applied microwave currents $I_{RF}>I_C$ the half-integer Shapiro steps may appear [93] if McCumber parameter $\beta_C=2\pi f_CR_NC\sim 1$. For the C-MS with d_1 = 6 nm, d_2 = 5.5 nm, and L = 10 μm measured at f_e=41 GHz, T = 4.2 K Figure 6b shows dependencies of normalized amplitudes of critical current, first Shapiro step and half-integer subharmonic step amplitudes vs. a. From these data we estimated q =0.13 in C-MS.

Preprints (www.preprints.org) | NOT PEER-REVIEWED | Posted: 9 May 2023 doi:10.20944/preprints202305.0597.v1

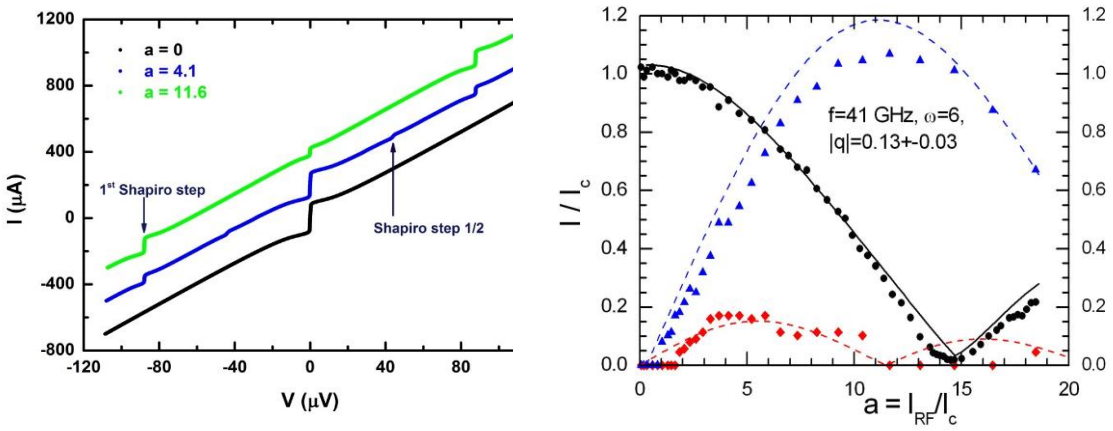

Figure 7. (a) Integer and fractional Shapiro steps in the *I-V* curves if monochromatic high frequency (41 GHz) radiation is applied. **(b)** Second harmonic of the superconducting current-phase relation $|q|=I_{c2}/I_{c1}$= -0.13 is calculated within Modified Resistive Shunted Junction (MRSJ) model [31,36].

High frequency dynamics of Josephson junctions with magnetic barriers depends also on propagation of electromagnetic waves. The influence of magnetic characteristics of Josephson junction barrier was considered and theoretically analyzed for S/I/F/S and S/F/I/F/S structures [84], as well for S/I_F/S [85], where F is a ferromagnet, and I_F is a ferromagnetic insulator. However, predicted deviations from ordinary theory [94] were not observed on S/I_F/S structures in experiments [95,96]. At the same time, the existence of strong SOI, which was not taken in-to account [84, 85], but exist in discussed S-MS structures may dramatically change high frequency the dynamics of electromagnetic waves propagation in Josephson strictures with magnetic barriers.

3.4. Resonance steps

In the case of S-MS the measurements of differential resistance dependences $R_D(V)$ under applied microwaves signal at fe= 50 GHz and different power P (see Figure 8a) showed sharp dips at the voltages $V_N = N \cdot (h/2e) \cdot fe$, demonstrating the equidistant character due to Shapiro steps. At the same time, the dips of normalized R_D/R_N values are different for opposite polarities of bias voltage V. Figure 8a also illustrates the dependence $R_D(V)$ measured without microwave radiation (see the top track in Fig.8a). It can be seen that even a weak microwave power P with a 30-dB decay smoothens the $R_D(V)$ dependence. Additional information at low power level of probe microwave signal can give the measurements of detector response function. Figure 8b show *I-V* curve and the voltage dependence of synchronous detector response obtained at f_e=50 GHz under P power weaker than that marked 30 dB in Fig.8a. It is seen that in addition to detector response function, strictly located at the voltage V-axis in correspondence to Josephson voltage-frequency relation, there exist other singularities. Switching off the microwave signal the singularities on *I-V* curve still took place. Applying an external magnetic field the singularities on $R_D(V)$ function changed the shape, keeping minima locations on V-axis fixed.

Preprints (www.preprints.org) | NOT PEER-REVIEWED | Posted: 9 May 2023 doi:10.20944/preprints202305.0597.v1

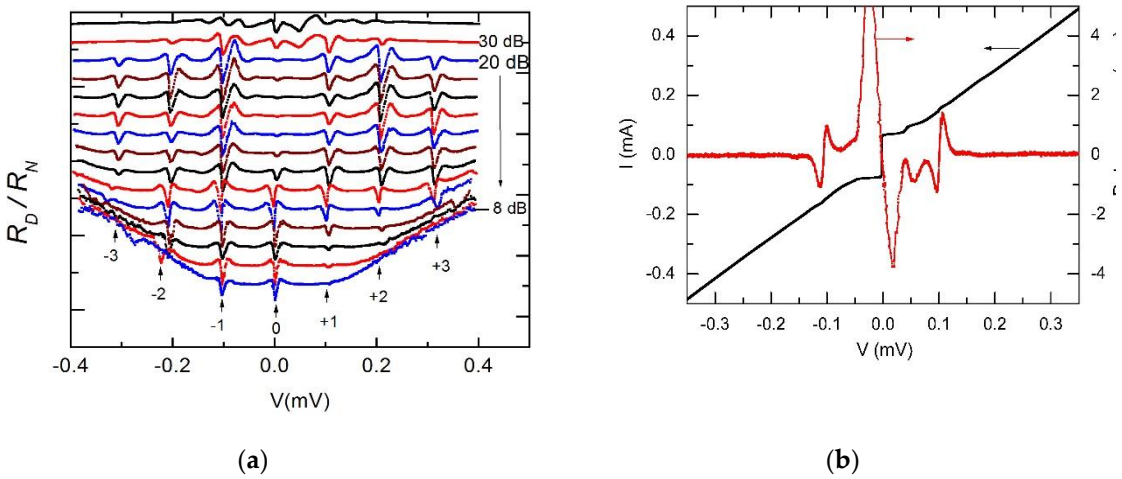

Figure 8. (a) Differential resistance R_D normalized to R_N versus voltage V under electromagnetic radiation at f=50.09 GHz for S-MS with L = 40 μm with a shift along the ordinate axis and an attenuator introduced decay in the radiation power P from 30 dB and further from 20 to 8 dB with a step of 1 dB. Arrows point Shapiro step numbers N, N=0 corresponds to the critical current. The top curve was measured without microwave radiation; **(b)** I-V curve and detector response at 50 GHz for S-MS with d=5 nm. Adopted from [80].

It is known that the influence of even weak magnetic field leads to appearance of resonant Fiske steps in I-V characteristic of a S/I/S tunnel junction (S is superconducting electrodes, and I is a non-magnetic insulator) [94,97] at voltages $V_k = n\Phi_0 c'/2L$, where k is the number of resonant step, Φ_0 is a magnetic flux quantum, $c' = c(t/\varepsilon\Lambda)^{1/2}$ is the Swihart velocity [98], c is the light velocity in vacuum, L is the junction width, t is the thickness of the insulator layer in the transmitting line with a dielectric permittivity ε, and Λ is the depth of magnetic field penetration into the layer and superconductors. In the case of a superconducting tunnel junction with an insulator characterized by magnetic properties, the penetration depth Λ becomes:

$$\Lambda = \mu t + \lambda_{L1} \operatorname{cotanh}(d_1/2\lambda_{L1}) + \lambda_{L2} \operatorname{cotanh}(d_2/2\lambda_{L2}) \quad (3),$$

where μ is the magnetic permeability, and d_i and λ_{Li} (i = 1, 2) are the thicknesses of superconducting films and their London magnetic field penetration depths, respectively. The existence of strong SOI in the insulator B-layer (I_{SO}) may change the dynamics of the propagation of electromagnetic waves in a S/I_{SO}/S structure The location of resonant current steps with respect to the dc voltage V were determined from the minima of the differential resistance $R_D = dV/dI$ of S-MS under the magnetic field H. The dependence of $R_D(V)$ at the magnetic field H = –1.3 Oe is shown in Figure 9a with the I-V curve. A difference in voltage positions of singularity on $R_D(V)$ took place at V_{+1} = 42 μV and V_{-1}= 51 μV marked by arrows. At voltages up to 200 μV (not shown in Figure 9a) differential resistance $R_D(V)$ demonstrates oscillations with magnetic field H which could be explain by the resonances Fiske steps at voltages V_k.

Figure 9b demonstrates magnetic field oscillating dependence of resonant current step amplitudes for numbers k=1, -1. Note, the asymmetry of V_k positions relative the voltage V=0 took place also for higher k numbers. Theoretical analysis of interaction of spin waves and plasma waves in Josephson junction with ferromagnetic insulator modeled as S/I/F/S or S/F/I/F/S media and its impact on Fiske singularities and a deviation from ordinary Fiske resonant behavior was made in [84,85]. The case of Josephson junction with a barrier made of antiferromagnetic insulator is less studied. It is worth to mention that spin waves in antiferromagnetic thin film has been examined in [99], and for antiferromagnetic spin dynamics in SIO [100].

Preprints (www.preprints.org) | NOT PEER-REVIEWED | Posted: 9 May 2023 doi:10.20944/preprints202305.0597.v1

Changing size L of S-MS the voltage positions V_k of resonances, as shown for the 1st and 2nd steps in Figure 9c, the Swihart velocity remained unchanged with a minor variation of expected V_kL products, confirming the Fiske type resonance origin. The stable V_k voltage positions against magnetic field for higher k-numbers are given in Figure 9d. Note again, Fiske resonances in Josephson junctions with ferromagnetic metallic barrier interlayers [95] did not demonstrate deviations of V_k voltage positions from theory [79]. A minor V_k shifts were noticed in paper [96] and were explained by an influence of electromagnetic surrounding of Josephson junction [101]. In our experimental case the registered in S-MS structures shifts of V_k positions are rather more pronounced. Taking the experimental Fiske resonance position V_1 allows us to estimate the Josephson junction's plasma frequency f_P~25 GHz which corresponds to dielectric constant ε~ 40 –45. This estimated value ε is of the same order of measured ones for SIO crystals [102] at higher temperatures than in our experiment and was explained by existence of Mott band and strong SOI properties [103] in Sr_2IrO_4.

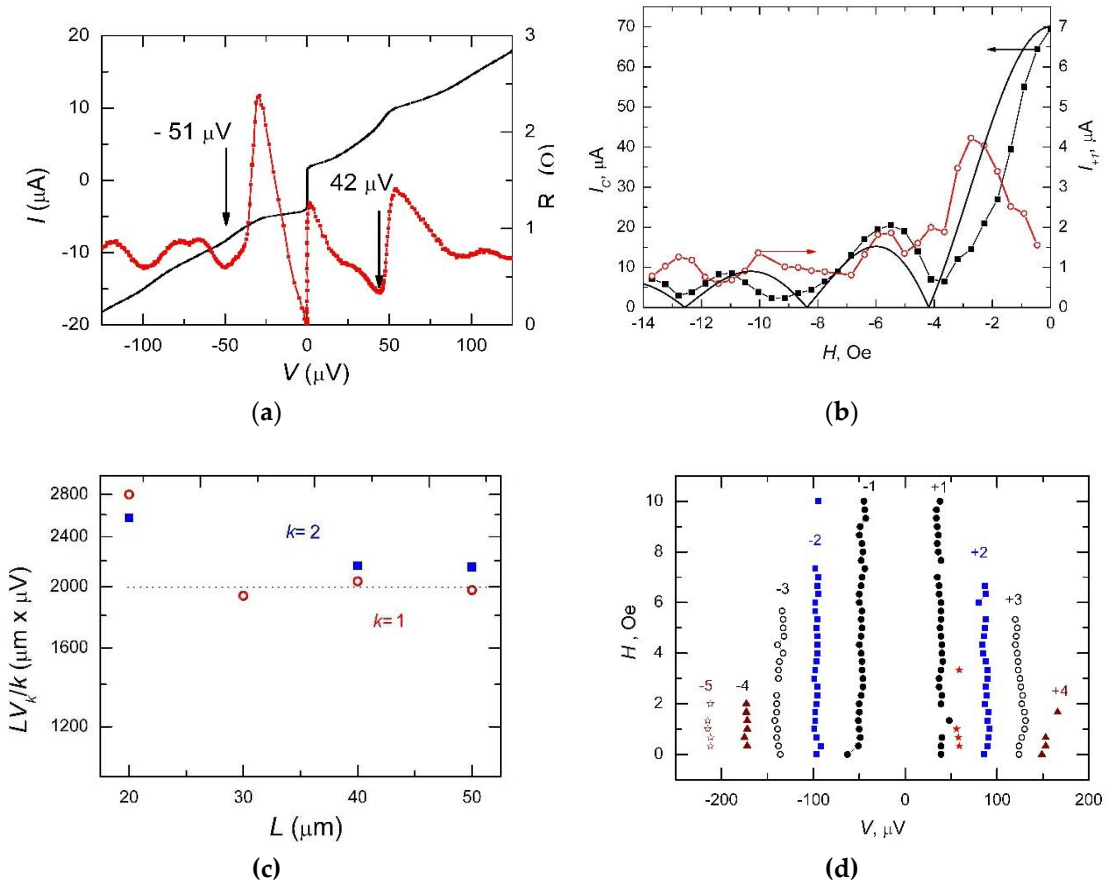

Figure 9. (a) *I-V* curve (black), and $R_D(V)$ (red) plotted at H= -2.7 Oe. Arrows point on Fiske resonance voltage positions for k=1; **(b)** Average critical current I_C = (I_{C+} + I_{C-})/2 (squares) and amplitude of Fiske steps $I_{+1}(H)$ versus magnetic field for k = +1 at V = +39 μV with theoretical Fraunhofer curve $I_C(H)$ (solid line); **(c)** The normalized by k the LV_k product vs. size L. Red symbols correspond to Fiske number k=1, blue to k=2. d)Fiske steps in the H–V plane with their numbers k. Adopted from [80,81].

3.5. Determination of the 2nd harmonic from CPR.

The information on CPR in a Josephson junction could be obtained from the dynamics of Shapiro steps by varying the power of microwave irradiation at high frequency limit f_e>f_C [38,55,64]. Calculations of both integer and half-integer Shapiro steps amplitudes were based on the Modified

Preprints (www.preprints.org) | NOT PEER-REVIEWED | Posted: 9 May 2023 doi:10.20944/preprints202305.0597.v1

Resistive Shunted Junction (MRSJ) model which takes into account the second harmonic of the CPR and the finite capacitance C of Josephson junction which determines the McCumber parameter $\beta_C>1$. In high-frequency limit $hf_e>2eI_cR_N$ the contribution of capacitance C on Shapiro step amplitude dependence vs. microwave power P (in terms of normalized RF current a [65]) is small and the shapes of the $I_C(a)$ and $I_1(a)$ dependences are mainly determined by the second harmonic of the CPR. If $q\neq0$ the amplitudes of $I_C(a)$, $I_1(a)$, $I_2(a)$, $I_3(a)$ etc. are equal to a sum of the Bessel functions J_n taken with different phases [65]:

$$I_n / Ic = 2\max_{\Theta}\left[J_n(x)\sin(\Theta) + qJ_{2n}(2x)\sin(2\Theta)\right], \quad (4)$$

where we search for a maximum of the expression in square brackets depending on shift of the phases Θ between Josephson self-generation and external oscillations at probe frequency f_e. In the equation (4) $x=a/\omega(\omega^2{}_{\beta_c}{}^2+1)^{1/2}$, $\omega=hf_e/2eI_cR_N$ is a normalized frequency and $a=I_\sim/I_C$ is a normalized amplitude of the external electromagnetic radiation [65]. As it follows from (4) in the case of large capacitance C or $\beta_C>1$ the amplitudes of Shapiro steps are changed. Using the equation (4) it is possible to calculate the q values from minima level of the experimental dependence $I_n(a)/I_c(0)$. At the first minimum ratio $q=I_c(a)/[I_c(0)J_0(2x)]$. The impact of both the capacitance C and second harmonic of the CPR initiate fractional Shapiro steps with the amplitudes:

$$I_{1/2} / I_c = 2\max_{\Theta}\left\{\sin(\Theta)\left[qJ_1(2x) + \beta_c\frac{J_1(x)J_0(x)}{(\beta_c\omega)^2/4+1} + 4q^2\beta_c\frac{J_2(2x)J_0(2x)}{(\beta_c\omega)^2+1}\cos(\Theta)\right]\right\} \quad (5)$$

There is a variable-sign expression in square brackets of the equation (5). Therefore, the $I_{1/2}(a)$ dependence differs from the case of Josephson junction with small capacitance ($\beta_C<1$): $I_{1/2}(a)\sim J_1(2a/\omega)$ [104]. The experimental data $I_{1/2}(a)$ can be fitted well if $q<0$. Negative q values (phase shift between first and second harmonics of the CPR) follows from theoretical calculations for S/S_d junctions with $\pi/4$ tilted c-axis of YBCO [87,105,106] and has been experimentally observed in bicrystal Josephson junctions [107]. However, even a small change of normalized frequency ω of the external electromagnetic radiation noticeably changes the shape of $I_{1/2}(a)$ dependence. This fact is explained by simultaneous influence on the process of fractional Shapiro step formation by the capacitance of Josephson junction and the second harmonic of the CPR $q\neq0$ (the two first members in (5) which have different signs. Note, usually the parameter β_C is determined from hysteresis on autonomous I-V curve without any external influence.

For studies not far from characteristic frequency $f_C=(I_CR_N)2e/h$ (h is Planck's constant) of Josephson junction the S-MS measurements at microwave frequencies were carried out mm wave frequency band: either at f_e=38 GHz, or f_e=50 GHz. The voltage dependence of differential resistance dV/dI under applied microwaves at f_e=50 GHz demonstrated both integer and fractional Shapiro steps which arise due to synchronization between Josephson self-oscillations and the external microwaves at voltages $V_{n,m}=(n/m)hf_e/2e$ [64]. Fractional Shapiro steps points on deviation from sin-type CPR and on the presence harmonics, particularly the second harmonic with $I_{C2}\neq0$. Figure 10a and Figure 10b show dependences of the first harmonic normalized amplitude $i_1=I_1/I_C$ (n=m=1), and the fractional (half-integer) $i_{1/2}=I_{1/2}/I_C$ (n=1, m=2) of Shapiro step vs. normalized microwave current $a=I_{MW}/I_C(0)$ at f_e=50 GHz. The dependences of $i_1(a)$ and $i_{1/2}(a)$ were calculated as well for different values of $q=I_{c2}/I_{c1}$ using the MRSJ model [46,102,106] and also are presented in Figure 10. Experimental data demonstrated well defined maximum for dependence $i_1(a)$ at microwave current $a\approx20$ and less pronounce maximum at $a\approx80$. Note, for $q>0$ the minima of theoretical function $i_1(a)$ do not reach level $i_1=0$. For $i_{1/2}(a)$ dependence of fractional ½ step it is seen that experimental minima are shifted from zero level within measurements uncertainty indicated by the error bar. Deviation of experimental $i_1(a)$ dependence from theoretical could be attributed to contribution of higher harmonics in CPR. Note, the impact of large microwave power on non-stationary processes is not considered in the modified MRSJ model. Taking the maximal experimental amplitude of $i_{1/2}(a)\approx0.3$ the best fit to theory for the half-integer Shapiro step corresponds to the theoretical function calculated for q=0.3. The d-wave symmetry of YBCO superconducting electrode with

Preprints (www.preprints.org) | NOT PEER-REVIEWED | Posted: 9 May 2023 doi:10.20944/preprints202305.0597.v1

order parameter amplitude Δ_d results in unconventional CPR with characteristic product of critical current -normal state resistance $I_{c2}R_N \approx \Gamma\,\Delta_{Nb}/e$ [58] The contribution of 2nd harmonic in CPR for a S/S$_d$ junction without interlayer barrier with the same electrical parameters as the discussed S-MS with L=40 μm gives I_{c2}≈20 nA for Γ =2·10^{-4}, Δ_{Nb}/e=0.8 mV and R_N =7.1 Ω at T=4.2 K. Note, using theoretical dependence for ratio I_{C1}/I_C vs. parameter q [65,89] and the estimated contribution of I_{c2} gives negligibly small estimate $q \approx 3\ 10^{-3}$. The deviation of CPR from sinusoidal may originate due to appearance of low energy states at the SIO/YBCO interface, related to the coherent Andreev reflections [62–64,109,110]. Indeed, the S-MS demonstrated the ZBCP at temperatures T=4.2 K and $T>T_{CNb}$ which are associated with Andreev low energy states. At low temperatures tunneling behavior of conductivity takes place also at higher voltages V>10 mV. An asymmetry of $G(V)$ dependence is also seen. Theoretical simulation [64] shows that the interface between cuprate superconductor S$_d$ and SIO interlayer film could exhibit the both helical Majorana fermions and zero-energy flat edge states. It is hard to prove existence of Majorana fermions, but observed the ZBCP tells infavor of theory [64]. However, the origin of the ZBCP and the asymmetry in $G(V)$ function in S-MS require additional studies.

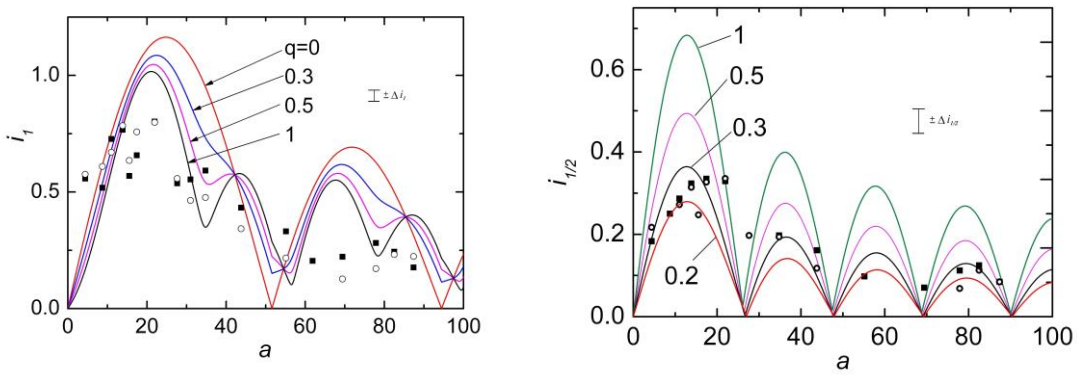

(**a**) (**b**)

Figure 10. **(a)** Normalized amplitudes of the first $i_1=I_1(a)/I_C(0)$ Shapiro step. Theoretical curves were calculated taking $a=I_{MW}/I_C$ as a fitting parameter for ratios $q=I_{C2}/I_{C1}$=0, 0.3, 0.5, 1 and McCumber parameter β_C=1. Error bar is indicated by $\pm\Delta i_1$; **(b)** Normalized amplitudes of half-integer Shapiro steps $i_{1/2}=I_{1/2}(a)/I_C(0)$. Error bar is indicated by $\pm\Delta i_{1/2}$. Theoretical curves were calculated for q= 0.2, 0.3, 0.5, 1 and β_C=1. Adopted from [80,81].

4. Conclusions

We have experimentally observed spin-triplet superconducting current in two types of hybrid Nb/B/YBa$_2$Cu$_3$O$_{7-x}$ junctions with different B-interlayer properties. In the case of B-interlayer comprised all-oxide ferromagnetic bilayer SrRuO$_3$/La$_{0.7}$Sr$_{0.3}$MnO$_3$ (composite mesa-structures, C-MS) the long-ranged superconducting correlations occur due non-collinear directions of magnetizations in the layers with a total thickness up 50 nm. In the second type of junctions, the B-interlayer was made of antiferromagnetic insulator Sr$_2$IrO$_4$ with strong spin-orbit interaction (spin-orbit mesa-structures, S-MS). Although the transparences of interfaces in C-MS and S-MS differ more than two orders, the both exhibit the a.c. Josephson effect, confirmed by Shapiro steps appearance, and the results of microwave detector response measurements. A deviation from ordinary superconducting current-phase relation $I_S(\varphi)$~sinφ was observed. Particularly, a ratio of the second harmonic relative the first harmonic $I_S(\varphi)$ up to 0.5 was registered for C-MS while the first harmonic should dominate in usual Josephson junctions. The robust nature of spin-triplet superconducting correlations against external magnetic field H was revealed in C-MS by an extraordinary slow decay of critical current $I_C(H)$ function with increasing H. In S-MS junctions with low interface transparences superconducting current was observed in junctions with B-interlayer thickness up to 7 nm. Strong spin-orbit interaction featured in appearance of zero-bias-conductance-peak and anomalous d.c. Josephson effect, performing unequal amplitudes of critical currents against change of current biasing polarity.

 doi:10.20944/preprints202305.0597.v1

Reducing the thickness of Sr_2IrO_4 interlayer to 5 nm results in appearance of resonant current steps inherent to Fiske resonance demonstrating oscillating behavior with magnetic field.

Author Contributions: Conceptualization, K.C. and G.O.; methodology, K.C. and Yu.K.; software, A.P.; validation, A.P. and Yu.K., resources, G.O.; data curation, A.P.; writing—original draft preparation, K.C.; writing—review and editing, G.O.; visualization, A.P.; supervision, G.O.; project administration, K.C.; funding acquisition, G.O. All authors have read and agreed to the published version of the manuscript.

Funding: The activity by G.O. on microwave measurements was partially supported by Russian Science Foundation (project No. 23-49-10006).

Acknowledgments: The authors acknowledge I.V. Borisenko, G. Cristiani, A.I. Kalabukhov, P.V. Komissinsky, G. Logvenov, A.V. Shadrin for sample fabrication, V.V. Demidov, A.E. Sheyerman for conducting experimental measurements, D. Winkler for the useful discussions.

Conflicts of Interest: The authors declare no conflict of interest

References

1. Bergeret, F. S.; Volkov, A. F.; Efetov, K. B. Long-Range Proximity Effects in Superconductor-Ferromagnet Structures. *Phys. Rev. Lett.* **2001**, *86* (18), 4096–4099. https://doi.org/10.1103/PhysRevLett.86.4096.
2. Robinson, J. W. A.; Witt, J. D. S.; Blamire, M. G. Controlled Injection of Spin-Triplet Supercurrents into a Strong Ferromagnet. *Science* **2010**, *329* (5987), 59–61. https://doi.org/10.1126/science.1189246.
3. Houzet, M.; Buzdin, A. I. Long Range Triplet Josephson Effect through a Ferromagnetic Trilayer. *Phys. Rev. B* **2007**, *76* (6), 060504. https://doi.org/10.1103/PhysRevB.76.060504.
4. Trifunovic, L. Long-Range Superharmonic Josephson Current. *Phys. Rev. Lett.* **2011**, *107* (4), 047001. https://doi.org/10.1103/PhysRevLett.107.047001.
5. Richard, C.; Houzet, M.; Meyer, J. S. Superharmonic Long-Range Triplet Current in a Diffusive Josephson Junction. *Phys. Rev.* Lett. **2013**, *110* (21), 217004. https://doi.org/10.1103/PhysRevLett.110.217004.
6. Sosnin, I.; Cho, H.; Petrashov, V. T.; Volkov, A. F. Superconducting Phase Coherent Electron Transport in Proximity Conical Ferromagnets. *Phys. Rev. Lett.* **2006**, *96* (15), 157002. https://doi.org/10.1103/PhysRevLett.96.157002.
7. Anwar, M. S.; Czeschka, F.; Hesselberth, M.; Porcu, M.; Aarts, J. Long-Range Supercurrents through Half-Metallic Ferromagnetic CrO_2. *Phys. Rev. B* **2010**, *82* (10), 100501. https://doi.org/10.1103/PhysRevB.82.100501.
8. Keizer, R. S.; Goennenwein, S. T. B.; Klapwijk, T. M.; Miao, G.; Xiao, G.; Gupta, A. A Spin Triplet Supercurrent through the Half-Metallic Ferromagnet CrO_2. *Nature* **2006**, *439* (7078), 825–827. https://doi.org/10.1038/nature04499.
9. Wang, J.; Singh, M.; Tian, M.; Kumar, N.; Liu, B.; Shi, C.; Jain, J. K.; Samarth, N.; Mallouk, T. E.; Chan, M. H. W. Interplay between Superconductivity and Ferromagnetism in Crystalline Nanowires. *Nat. Phys.* **2010**, *6* (5), 389–394. https://doi.org/10.1038/nphys1621.
10. Sprungmann, D.; Westerholt, K.; Zabel, H.; Weides, M.; Kohlstedt, H. Evidence for Triplet Superconductivity in Josephson Junctions with Barriers of the Ferromagnetic Heusler Alloy Cu_2MnAl. *Phys. Rev. B* **2010**, *82* (6), 060505. https://doi.org/10.1103/PhysRevB.82.060505.
11. Klose, C.; Khaire, T. S.; Wang, Y.; Pratt, W. P.; Birge, N. O.; McMorran, B. J.; Ginley, T. P.; Borchers, J. A.; Kirby, B. J.; Maranville, B. B.; Unguris, J. Optimization of Spin-Triplet Supercurrent in Ferromagnetic Josephson Junctions. *Phys. Rev. Lett.* **2012**, *108* (12), 127002. https://doi.org/10.1103/PhysRevLett.108.127002.
12. Khaire, T. S.; Khasawneh, M. A.; Pratt, W. P.; Birge, N. O. Observation of Spin-Triplet Superconductivity in Co-Based Josephson Junctions. *Phys. Rev. Lett.* **2010**, *104* (13), 137002. https://doi.org/10.1103/PhysRevLett.104.137002.
13. Bousquet, E.; Dawber, M.; Stucki, N.; Lichtensteiger, C.; Hermet, P.; Gariglio, S.; Triscone, J.-M.; Ghosez, P. Improper Ferroelectricity in Perovskite Oxide Artificial Superlattices. *Nature* **2008**, *452* (7188), 732–736. https://doi.org/10.1038/nature06817.
14. Ohta, H.; Kim, S.; Mune, Y.; Mizoguchi, T.; Nomura, K.; Ohta, S.; Nomura, T.; Nakanishi, Y.; Ikuhara, Y.; Hirano, M.; Hosono, H.; Koumoto, K. Giant Thermoelectric Seebeck Coefficient of a Two-Dimensional Electron Gas in $SrTiO_3$. *Nat. Mater.* **2007**, *6* (2), 129–134. https://doi.org/10.1038/nmat1821.
15. Ohtomo, A.; Hwang, H. Y. A High-Mobility Electron Gas at the $LaAlO_3/SrTiO_3$ Heterointerface. *Nature* **2004**, *427* (6973), 423–426. https://doi.org/10.1038/nature02308.

16. Chen, Y. Z.; Trier, F.; Wijnands, T.; Green, R. J.; Gauquelin, N.; Egoavil, R.; Christensen, D. V.; Koster, G.; Huijben, M.; Bovet, N.; Macke, S.; He, F.; Sutarto, R.; Andersen, N. H.; Sulpizio, J. A.; Honig, M.; Prawiroatmodjo, G. E. D. K.; Jespersen, T. S.; Linderoth, S.; Ilani, S.; Verbeeck, J.; Van Tendeloo, G.; Rijnders, G.; Sawatzky, G. A.; Pryds, N. Extreme Mobility Enhancement of Two-Dimensional Electron Gases at Oxide Interfaces by Charge-Transfer-Induced Modulation Doping. *Nat. Mater.* **2015**, *14* (8), 801–806. https://doi.org/10.1038/nmat4303.
17. Trier, F.; Prawiroatmodjo, G. E. D. K.; Zhong, Z.; Christensen, D. V.; von Soosten, M.; Bhowmik, A.; Lastra, J. M. G.; Chen, Y.; Jespersen, T. S.; Pryds, N. Quantization of Hall Resistance at the Metallic Interface between an Oxide Insulator and $SrTiO_3$. *Phys. Rev. Lett.* **2016**, *117* (9), 096804. https://doi.org/10.1103/PhysRevLett.117.096804.
18. Dagotto, E.; Hotta, T.; Moreo, A. Colossal Magnetoresistant Materials: The Key Role of Phase Separation. *Phys. Rep.* **2001**, *344* (1–3), 1–153. https://doi.org/10.1016/S0370-1573(00)00121-6.
19. Kalcheim, Y.; Kirzhner, T.; Koren, G.; Millo, O. Long-Range Proximity Effect in $La_{2/3}Ca_{1/3}MnO_3$/(100)$YBa_2Cu_3O_{7-\delta}$ Ferromagnet/Superconductor Bilayers: Evidence for Induced Triplet Superconductivity in the Ferromagnet. *Phys. Rev. B* **2011**, *83* (6), 064510. https://doi.org/10.1103/PhysRevB.83.064510.
20. Visani, C.; Sefrioui, Z.; Tornos, J.; Leon, C.; Briatico, J.; Bibes, M.; Barthélémy, A.; Santamaría, J.; Villegas, J. E. Equal-Spin Andreev Reflection and Long-Range Coherent Transport in High-Temperature Superconductor/Half-Metallic Ferromagnet Junctions. *Nat. Phys.* **2012**, *8* (7), 539–543. https://doi.org/10.1038/nphys2318.
21. van Zalk, M.; Brinkman, A.; Aarts, J.; Hilgenkamp, H. Interface Resistance of $YBa_2Cu_3O_{7-\delta}$ / $La_{0.67}Sr_{0.33}MnO_3$ Ramp-Type Contacts. *Phys. Rev. B* **2010**, *82* (13), 134513. https://doi.org/10.1103/PhysRevB.82.134513.
22. Petrzhik, A. M.; Ovsyannikov, G. A.; Shadrin, A. V.; Konstantinyan, K. I.; Zaitsev, A. V.; Demidov, V. V.; Kislinskii, Yu. V. Electron Transport in Hybrid Superconductor Heterostructures with Manganite Interlayers. *J. Exp. Theor. Phys.* **2011**, *112* (6), 1042–1050. https://doi.org/10.1134/S1063776111050177.
23. Volkov, A. F.; Efetov, K. B. Odd Spin-Triplet Superconductivity in a Multilayered Superconductor-Ferromagnet Josephson Junction. *Phys. Rev. B* **2010**, *81* (14), 144522. https://doi.org/10.1103/PhysRevB.81.144522.
24. Khasawneh, M. A.; Khaire, T. S.; Klose, C.; Pratt Jr, W. P.; Birge, N. O. Spin-Triplet Supercurrent in Co-Based Josephson Junctions. *Supercond. Sci. Technol.* **2011**, *24* (2), 024005. https://doi.org/10.1088/0953-2048/24/2/024005.
25. Leksin, P. V.; Garif'yanov, N. N.; Garifullin, I. A.; Fominov, Ya. V.; Schumann, J.; Krupskaya, Y.; Kataev, V.; Schmidt, O. G.; Büchner, B. Evidence for Triplet Superconductivity in a Superconductor-Ferromagnet Spin Valve. *Phys. Rev. Lett.* **2012**, *109* (5), 057005. https://doi.org/10.1103/PhysRevLett.109.057005.
26. Zdravkov, V. I.; Kehrle, J.; Obermeier, G.; Lenk, D.; Krug von Nidda, H.-A.; Müller, C.; Kupriyanov, M. Yu.; Sidorenko, A. S.; Horn, S.; Tidecks, R.; Tagirov, L. R. Experimental Observation of the Triplet Spin-Valve Effect in a Superconductor-Ferromagnet Heterostructure. *Phys. Rev. B* **2013**, *87* (14), 144507. https://doi.org/10.1103/PhysRevB.87.144507.
27. Trifunovic, L.; Popović, Z.; Radović, Z. Josephson Effect and Spin-Triplet Pairing Correlations in S F1 F2 S Junctions. *Phys. Rev. B* **2011**, *84* (6), 064511. https://doi.org/10.1103/PhysRevB.84.064511.
28. Sperstad, I. B.; Linder, J.; Sudbø, A. Josephson Current in Diffusive Multilayer Superconductor/Ferromagnet/Superconductor Junctions. *Phys. Rev. B* **2008**, *78* (10), 104509. https://doi.org/10.1103/PhysRevB.78.104509.
29. Knežević, M.; Trifunovic, L.; Radović, Z. Signature of the Long Range Triplet Proximity Effect in the Density of States. *Phys. Rev. B* **2012**, *85* (9), 094517. https://doi.org/10.1103/PhysRevB.85.094517.
30. Pal, A.; Barber, Z. H.; Robinson, J. W. A.; Blamire, M. G. Pure Second Harmonic Current-Phase Relation in Spin-Filter Josephson Junctions. *Nat. Commun.* **2014**, *5* (1), 3340. https://doi.org/10.1038/ncomms4340.
31. Ovsyannikov, G. A.; Sheyerman, A. E.; Shadrin, A. V.; Kislinskii, Yu. V.; Constantinian, K. Y.; Kalabukhov, A. Triplet Superconducting Correlations in Oxide Heterostructures with a Composite Ferromagnetic Interlayer. *JETP Lett.* **2013**, *97* (3), 145–148. https://doi.org/10.1134/S0021364013030089.
32. Khaydukov, Yu. N.; Ovsyannikov, G. A.; Sheyerman, A. E.; Constantinian, K. Y.; Mustafa, L.; Keller, T.; Uribe-Laverde, M. A.; Kislinskii, Yu. V.; Shadrin, A. V.; Kalaboukhov, A.; Keimer, B.; Winkler, D. Evidence for Spin-Triplet Superconducting Correlations in Metal-Oxide Heterostructures with Noncollinear Magnetization. *Phys. Rev. B* **2014**, *90* (3), 035130. https://doi.org/10.1103/PhysRevB.90.035130.
33. Sheyerman, A.; Ovsyannikov, G.; Kislinskii, Y.; Constantinian, K.; Shadrin, A. Current-Phase Relation of Superconductor-Ferromagnet-Superconductor Junctions with a Composite Interlayer. *Solid State Phenom.* **2015**, *233–234*, 737–740. https://doi.org/10.4028/www.scientific.net/SSP.233-234.737.

34. Sheyerman, A. E.; Constantinian, K. Y.; Ovsyannikov, G. A.; Kislinskii, Yu. V.; Shadrin, A. V.; Kalabukhov, A. V.; Khaydukov, Yu. N. Spin-Triplet Electron Transport in Hybrid Superconductor Heterostructures with a Composite Ferromagnetic Interlayer. *J. Exp. Theor. Phys.* **2015**, *120* (6), 1024–1033. https://doi.org/10.1134/S1063776115050192.
35. Ovsyannikov, G. A.; Constantinian, K. Y.; Demidov, V. V.; Khaydukov, Yu. N. Magnetic Proximity Effect and Superconducting Triplet Correlations at the Cuprate Superconductor and Oxide Spin Valve Interface. *Low Temp. Phys.* **2016**, *42* (10), 873–883. https://doi.org/10.1063/1.4966622.
36. Constantinian, K.; Ovsyannikov, G.; Kislinskii, Y.; Sheyerman, A.; Shadrin, A.; Kalabukhov, A.; Mustafa, L.; Khaydukov, Y.; Winkler, D. Spin-Triplet Superconducting Current in Metal-Oxide Heterostructures with Composite Ferromagnetic Interlayer. *IEEE Trans. Appl. Supercond.* **2016**, 1–1. https://doi.org/10.1109/TASC.2016.2522300.
37. Eschrig, M. Spin-Polarized Supercurrents for Spintronics: A Review of Current Progress. *Rep. Prog. Phys.* **2015**, *78* (10), 104501. https://doi.org/10.1088/0034-4885/78/10/104501.
38. Linder, J.; Robinson, J. W. A. Superconducting Spintronics. *Nat. Phys.* **2015**, *11* (4), 307–315. https://doi.org/10.1038/nphys3242.
39. Horsdal, M.; Khaliullin, G.; Hyart, T.; Rosenow, B. Enhancing Triplet Superconductivity by the Proximity to a Singlet Superconductor in Oxide Heterostructures. *Phys. Rev. B* **2016**, *93* (22), 220502. https://doi.org/10.1103/PhysRevB.93.220502.
40. Bergeret, F. S.; Tokatly, I. V. Spin-Orbit Coupling as a Source of Long-Range Triplet Proximity Effect in Superconductor-Ferromagnet Hybrid Structures. *Phys. Rev. B* **2014**, *89* (13), 134517. https://doi.org/10.1103/PhysRevB.89.134517.
41. Jacobsen, S. H.; Linder, J. Giant Triplet Proximity Effect in π-Biased Josephson Junctions with Spin-Orbit Coupling. *Phys. Rev. B* **2015**, *92* (2), 024501. https://doi.org/10.1103/PhysRevB.92.024501.
42. Konschelle, F. Transport Equations for Superconductors in the Presence of Spin Interaction. *Eur. Phys. J. B* **2014**, *87* (5), 119. https://doi.org/10.1140/epjb/e2014-50143-0.
43. Bergeret, F. S.; Volkov, A. F.; Efetov, K. B. Odd Triplet Superconductivity and Related Phenomena in Superconductor-Ferromagnet Structures. *Rev. Mod. Phys.* **2005**, *77* (4), 1321–1373. https://doi.org/10.1103/RevModPhys.77.1321.
44. Bobkova, I. V.; Bobkov, A. M. Quasiclassical Theory of Magnetoelectric Effects in Superconducting Heterostructures in the Presence of Spin-Orbit Coupling. *Phys. Rev. B* **2017**, *95* (18), 184518. https://doi.org/10.1103/PhysRevB.95.184518.
45. Reeg, C. R.; Maslov, D. L. Proximity-Induced Triplet Superconductivity in Rashba Materials. *Phys. Rev. B* **2015**, *92* (13), 134512. https://doi.org/10.1103/PhysRevB.92.134512.
46. Yano, R.; Koyanagi, M.; Kashiwaya, H.; Tsumura, K.; Hirose, H. T.; Sasagawa, T.; Asano, Y.; Kashiwaya, S. Unusual Superconducting Proximity Effect in Magnetically Doped Topological Josephson Junctions. *J. Phys. Soc. Jpn.* **2020**, *89* (3), 034702. https://doi.org/10.7566/JPSJ.89.034702.
47. Sau, J. D.; Lutchyn, R. M.; Tewari, S.; Das Sarma, S. Generic New Platform for Topological Quantum Computation Using Semiconductor Heterostructures. *Phys. Rev. Lett.* **2010**, *104* (4), 040502. https://doi.org/10.1103/PhysRevLett.104.040502.
48. Suominen, H. J.; Danon, J.; Kjaergaard, M.; Flensberg, K.; Shabani, J.; Palmstrøm, C. J.; Nichele, F.; Marcus, C. M. Anomalous Fraunhofer Interference in Epitaxial Superconductor-Semiconductor Josephson Junctions. *Phys. Rev. B* **2017**, *95* (3), 035307. https://doi.org/10.1103/PhysRevB.95.035307.
49. Domínguez, F.; Kashuba, O.; Bocquillon, E.; Wiedenmann, J.; Deacon, R. S.; Klapwijk, T. M.; Platero, G.; Molenkamp, L. W.; Trauzettel, B.; Hankiewicz, E. M. Josephson Junction Dynamics in the Presence of 2 π - and 4 π - Periodic Supercurrents. *Phys. Rev. B* **2017**, *95* (19), 195430. https://doi.org/10.1103/PhysRevB.95.195430.
50. Wiedenmann, J.; Bocquillon, E.; Deacon, R. S.; Hartinger, S.; Herrmann, O.; Klapwijk, T. M.; Maier, L.; Ames, C.; Brüne, C.; Gould, C.; Oiwa, A.; Ishibashi, K.; Tarucha, S.; Buhmann, H.; Molenkamp, L. W. 4π-Periodic Josephson Supercurrent in HgTe-Based Topological Josephson Junctions. *Nat. Commun.* **2016**, *7* (1), 10303. https://doi.org/10.1038/ncomms10303.
51. Pedder, C. J.; Meng, T.; Tiwari, R. P.; Schmidt, T. L. Missing Shapiro Steps and the 8 π -Periodic Josephson Effect in Interacting Helical Electron Systems. *Phys. Rev. B* **2017**, *96* (16), 165429. https://doi.org/10.1103/PhysRevB.96.165429.
52. Moon, S. J.; Jin, H.; Kim, K. W.; Choi, W. S.; Lee, Y. S.; Yu, J.; Cao, G.; Sumi, A.; Funakubo, H.; Bernhard, C.; Noh, T. W. Dimensionality-Controlled Insulator-Metal Transition and Correlated Metallic State in 5 d Transition Metal Oxides $Sr_{n+1}Ir_nO_{3n+1}$ (n = 1 , 2, and ∞). *Phys. Rev. Lett.* **2008**, *101* (22), 226402. https://doi.org/10.1103/PhysRevLett.101.226402.

53. Witczak-Krempa, W.; Chen, G.; Kim, Y. B.; Balents, L. Correlated Quantum Phenomena in the Strong Spin-Orbit Regime. *Annu. Rev. Condens. Matter Phys.* **2014**, *5* (1), 57–82. https://doi.org/10.1146/annurev-conmatphys-020911-125138.
54. Schaffer, R.; Kin-Ho Lee, E.; Yang, B.-J.; Kim, Y. B. Recent Progress on Correlated Electron Systems with Strong Spin–Orbit Coupling. *Rep. Prog. Phys.* **2016**, *79* (9), 094504. https://doi.org/10.1088/0034-4885/79/9/094504.
55. Gordon, E. E.; Xiang, H.; Köhler, J.; Whangbo, M.-H. Spin Orientations of the Spin-Half Ir^{4+} Ions in Sr_3NiIrO_6, Sr_2IrO_4, and Na_2IrO_3 : Density Functional, Perturbation Theory, and Madelung Potential Analyses. *J. Chem. Phys.* **2016**, *144* (11), 114706. https://doi.org/10.1063/1.4943889.
56. Gim, Y.; Sethi, A.; Zhao, Q.; Mitchell, J. F.; Cao, G.; Cooper, S. L. Isotropic and Anisotropic Regimes of the Field-Dependent Spin Dynamics in Sr_2IrO_4 : Raman Scattering Studies. *Phys. Rev. B* **2016**, *93* (2), 024405. https://doi.org/10.1103/PhysRevB.93.024405.
57. Kim, Y. K.; Sung, N. H.; Denlinger, J. D.; Kim, B. J. Observation of a D-Wave Gap in Electron-Doped Sr2IrO4. *Nat. Phys.* **2016**, *12* (1), 37–41. https://doi.org/10.1038/nphys3503.
58. Hikino, S. Magnetization Reversal by Tuning Rashba Spin–Orbit Interaction and Josephson Phase in a Ferromagnetic Josephson Junction. *J. Phys. Soc. Jpn.* **2018**, *87* (7), 074707. https://doi.org/10.7566/JPSJ.87.074707.
59. Ovsyannikov, G. A.; Grishin, A. S.; Constantinian, K. Y.; Shadrin, A. V.; Petrzhik, A. M.; Kislinskii, Yu. V.; Cristiani, G.; Logvenov, G. Superconducting Heterostructures Interlayered with a Material with Strong Spin–Orbit Interaction. *Phys. Solid State* **2018**, *60* (11), 2166–2172. https://doi.org/10.1134/S1063783418110227.
60. Petrzhik, A. M.; Cristiani, G.; Logvenov, G.; Pestun, A. E.; Andreev, N. V.; Kislinskii, Yu. V.; Ovsyannikov, G. A. Growth Technology and Characteristics of Thin Strontium Iridate Films and Iridate–Cuprate Superconductor Heterostructures. *Tech. Phys. Lett.* **2017**, *43* (6), 554–557. https://doi.org/10.1134/S1063785017060244.
61. Wang, H.; Yu, S.-L.; Li, J.-X. Fermi Arcs, Pseudogap, and Collective Excitations in Doped Sr_2IrO_4: A Generalized Fluctuation Exchange Study. *Phys. Rev. B* **2015**, *91* (16), 165138. https://doi.org/10.1103/PhysRevB.91.165138.
62. Takei, S.; Fregoso, B. M.; Galitski, V.; Das Sarma, S. Topological Superconductivity and Majorana Fermions in Hybrid Structures Involving Cuprate High-Tc Superconductors. *Phys. Rev. B* **2013**, *87* (1), 014504. https://doi.org/10.1103/PhysRevB.87.014504.
63. Chen, Y.; Kee, H.-Y. Helical Majorana Fermions and Flat Edge States in the Heterostructures of Iridates and High-T_C Cuprates. *Phys. Rev. B* **2018**, *97* (8), 085155. https://doi.org/10.1103/PhysRevB.97.085155.
64. Petrzhik, A. M.; Constantinian, K. Y.; Ovsyannikov, G. A.; Zaitsev, A. V.; Shadrin, A. V.; Grishin, A. S.; Kislinski, Yu. V.; Cristiani, G.; Logvenov, G. Superconducting Current and Low-Energy States in a Mesa-Heterostructure Interlayered with a Strontium Iridate Film with Strong Spin-Orbit Interaction. *Phys. Rev. B* **2019**, *100* (2), 024501. https://doi.org/10.1103/PhysRevB.100.024501.
65. Komissinskiy, P.; Ovsyannikov, G. A.; Constantinian, K. Y.; Kislinski, Y. V.; Borisenko, I. V.; Soloviev, I. I.; Kornev, V. K.; Goldobin, E.; Winkler, D. High-Frequency Dynamics of Hybrid Oxide Josephson Heterostructures. *Phys. Rev. B* **2008**, *78* (2), 024501. https://doi.org/10.1103/PhysRevB.78.024501.
66. Ovsyannikov, G. A.; Petrzhik, A. M.; Borisenko, I. V.; Klimov, A. A.; Ignatov, Yu. A.; Demidov, V. V.; Nikitov, S. A. Magnetotransport Characteristics of Strained $La_{0.7}Sr_{0.3}MnO_3$ Epitaxial Manganite Films. *J. Exp. Theor. Phys.* **2009**, *108* (1), 48–55. https://doi.org/10.1134/S1063776109010075.
67. Izyumov, Y. A.; Skryabin, Y. N. Double Exchange Model and the Unique Properties of the Manganites. *Phys.-Uspekhi* **2001**, *44* (2), 109–134. https://doi.org/10.1070/PU2001v044n02ABEH000840.
68. Huang, Q.; Santoro, A.; Lynn, J. W.; Erwin, R. W.; Borchers, J. A.; Peng, J. L.; Greene, R. L. Structure and Magnetic Order in Undoped Lanthanum Manganite. *Phys. Rev. B* **1997**, *55* (22), 14987–14999. https://doi.org/10.1103/PhysRevB.55.14987.
69. Fita, I. M.; Szymczak, R.; Baran, M.; Markovich, V.; Puzniak, R.; Wisniewski, A.; Shiryaev, S. V.; Varyukhin, V. N.; Szymczak, H. Evolution of Ferromagnetic Order in $LaMnO_{3.05}$ Single Crystals: Common Origin of Both Pressure and Self-Doping Effects. *Phys. Rev. B* **2003**, *68* (1), 014436. https://doi.org/10.1103/PhysRevB.68.014436.
70. Mieville, L.; Worledge, D.; Geballe, T. H.; Contreras, R.; Char, K. Transport across Conducting Ferromagnetic Oxide/Metal Interfaces. *Appl. Phys. Lett.* **1998**, *73* (12), 1736–1738. https://doi.org/10.1063/1.122261.
71. Constantinian, K. Y.; Ovsyannikov, G. A.; Shadrin, A. V.; Kislinski, Y. V.; Petrzhik, A. M.; Kalaboukhov, A. S. Hybrid superconducting heterostructures with magnetic interlayers. *Radioelectron. Nanosyst. Inf. Technol.* **2021**, *13* (4), 471–478. https://doi.org/10.17725/rensit.2021.13.471.

72. Kashiwaya, S.; Tanaka, Y. Tunnelling Effects on Surface Bound States in Unconventional Superconductors. *Rep. Prog. Phys.* **2000**, *63* (10), 1641–1724. https://doi.org/10.1088/0034-4885/63/10/202.
73. Petković, I.; Aprili, M.;. Barnes, S. E.; Beuneu, F.; Maekawa, S. Direct dynamical coupling of spin modes and singlet Josephson supercurrent in ferromagnetic Josephson junctions. *Phys. Rev. B* **2009**, *80* (22), 220502(R). https://doi.org/10.1103/PhysRevB.80.220502.
74. Ryazanov, V. V.; Oboznov, V. A.; Rusanov, A. Yu.; Veretennikov, A. V.; Golubov, A. A.; Aarts, J. Coupling of Two Superconductors through a Ferromagnet: Evidence for a π Junction. *Phys. Rev. Lett.* **2001**, *86* (11), 2427-2430. https://doi.org/10.1103/PhysRevLett.86.2427.
75. Cohn, J. L.; Neumeier, J. J.; Popoviciu, C. P.; McClellan, K. J.; Leventouri, Th. Local Lattice Distortions and Thermal Transport in Perovskite Manganites. *Phys. Rev. B* **1997**, *56* (14), R8495–R8498. https://doi.org/10.1103/PhysRevB.56.R8495.
76. Kostic, P.; Okada, Y.; Collins, N. C.; Schlesinger, Z.; Reiner, J. W.; Klein, L.; Kapitulnik, A.; Geballe, T. H.; Beasley, M. R. Non-Fermi-Liquid Behavior of SrRuO 3 : Evidence from Infrared Conductivity. *Phys. Rev. Lett.* **1998**, *81* (12), 2498–2501. https://doi.org/10.1103/PhysRevLett.81.2498.
77. Woodfield, B. F.; Wilson, M. L.; Byers, J. M. Low-Temperature Specific Heat of $La_{1-x}Sr_xMnO_{3+\delta}$. *Phys. Rev. Lett.* **1997**, *78* (16).
78. Asulin, I.; Yuli, O.; Koren, G.; Millo, O. Evidence for Induced Magnetization in Superconductor-Ferromagnet Heterostructures: A Scanning Tunneling Spectroscopy Study. *Phys. Rev. B* **2009**, *79* (17), 174524. https://doi.org/10.1103/PhysRevB.79.174524.
79. Antonio Barone, G. P. *Physics and Applications of the Josephson Effect*; Wiley: New York, 2005.
80. Constantinian, K. Y.; Ovsyannikov, G. A.; Petrzhik, A. M.; Shadrin, A. V.; Kislinskii, Yu. V.; Cristiani, G.; Logvenov, G. Resonant Current Steps in Josephson Structures with a Layer from a Material with Strong Spin–Orbit Interaction. *Phys. Solid State* **2020**, *62* (9), 1549–1553. https://doi.org/10.1134/S1063783420090152.
81. Constantinian, K. Y.; Petrzhik, A. M.; Ovsyannikov, G. A.; Shadrin, A. V.; Kislinskii, Y. V.; Cristiani, G.; Logvenov, G. Superconducting Heterostructure with Barrier with Strong Spin-Orbit Interaction. *J. Phys. Conf. Ser.* **2020**, *1559* (1), 012023. https://doi.org/10.1088/1742-6596/1559/1/012023.
82. Silaev, M. A.; Tokatly, I. V.; Bergeret, F. S. Anomalous Current in Diffusive Ferromagnetic Josephson Junctions. *Phys. Rev. B* **2017**, *95* (18), 184508. https://doi.org/10.1103/PhysRevB.95.184508.
83. Calder, S.; Pajerowski, D. M.; Stone, M. B.; May, A. F. Spin-Gap and Two-Dimensional Magnetic Excitations in Sr_2IrO_4. *Phys. Rev. B* **2018**, *98* (22), 220402. https://doi.org/10.1103/PhysRevB.98.220402.
84. Mai, S.; Kandelaki, E.; Volkov, A. F.; Efetov, K. B. Interaction of Josephson and Magnetic Oscillations in Josephson Tunnel Junctions with a Ferromagnetic Layer. *Phys. Rev. B* **2011**, *84* (14), 144519. https://doi.org/10.1103/PhysRevB.84.144519.
85. Hikino, S.; Mori, M.; Maekawa, S. Zero-Field Fiske Resonance Coupled with Spin-Waves in Ferromagnetic Josephson Junctions. *J. Phys. Soc. Jpn.* **2014**, *83* (7), 074704. https://doi.org/10.7566/JPSJ.83.074704.
86. Komissinski, P. V.; Il'ichev, E.; Ovsyannikov, G. A.; Kovtonyuk, S. A.; Grajcar, M.; Hlubina, R.; Ivanov, Z.; Tanaka, Y.; Yoshida, N.; Kashiwaya, S. Observation of the Second Harmonic in Superconducting Current-Phase Relation of Nb/Au/(001)$YBa_2Cu_3O_x$ Heterojunctions. *Europhys. Lett. EPL* **2002**, *57* (4), 585–591. https://doi.org/10.1209/epl/i2002-00501-8.
87. Blais, A.; Zagoskin, A. M. Operation of Universal Gates in a Solid-State Quantum Computer Based on Clean Josephson Junctions between ***d*** - Wave Superconductors. *Phys. Rev. A* **2000**, *61* (4), 042308. https://doi.org/10.1103/PhysRevA.61.042308.
88. Tanaka, Y.; Kashiwaya, S. Theory of the Josephson Effect in d -Wave Superconductors. *Phys. Rev. B* **1996**, *53* (18), R11957–R11960. https://doi.org/10.1103/PhysRevB.53.R11957.
89. Goldobin, E.; Koelle, D.; Kleiner, R.; Buzdin, A. Josephson Junctions with Second Harmonic in the Current-Phase Relation: Properties of φ Junctions. *Phys. Rev. B* **2007**, *76* (22), 224523. https://doi.org/10.1103/PhysRevB.76.224523.
90. Petrzhik, A. M.; Ovsyannikov, G. A.; Shadrin, A. V.; Konstantinyan, K. I.; Zaitsev, A. V.; Demidov, V. V.; Kislinskii, Yu. V. Electron Transport in Hybrid Superconductor Heterostructures with Manganite Interlayers. *J. Exp. Theor. Phys.* **2011**, *112* (6), 1042–1050. https://doi.org/10.1134/S1063776111050177.
91. Korneta, O. B.; Qi, T.; Chikara, S.; Parkin, S.; De Long, L. E.; Schlottmann, P.; Cao, G. Electron-Doped $Sr_2IrO_{4-\delta}$ ($0 \le \delta \le 0.04$) : Evolution of a Disordered $J_{eff} = 1/2$ Mott Insulator into an Exotic Metallic State. *Phys. Rev. B* **2010**, *82* (11), 115117. https://doi.org/10.1103/PhysRevB.82.115117.
92. Horsdal, M.; Hyart, T. Robust Semi-Dirac Points and Unconventional Topological Phase Transitions in Doped Superconducting Sr_2IrO_4 Tunnel Coupled to t2g Electron Systems. *SciPost Phys.* **2017**, *3* (6), 041. https://doi.org/10.21468/SciPostPhys.3.6.041.

 doi:10.20944/preprints202305.0597.v1

93. Seidel, P.; Siegel, M.; Heinz, E. Microwave-Induced Steps in High-Tc Josephson Junctions. *Phys. C Supercond.* **1991**, *180* (1–4), 284–287. https://doi.org/10.1016/0921-4534(91)90682-O.
94. Coon, D. D.; Fiske, M. D. Josephson Ac and Step Structure in the Supercurrent Tunneling Characteristic. *Phys. Rev.* **1965**, *138* (3A), A744–A746. https://doi.org/10.1103/PhysRev.138.A744.
95. Wild, G.; Probst, C.; Marx, A.; Gross, R. Josephson Coupling and Fiske Dynamics in Ferromagnetic Tunnel Junctions. *Eur. Phys. J. B* **2010**, *78* (4), 509–523. https://doi.org/10.1140/epjb/e2010-10636-4.
96. Pfeiffer, J.; Kemmler, M.; Koelle, D.; Kleiner, R.; Goldobin, E.; Weides, M.; Feofanov, A. K.; Lisenfeld, J.; Ustinov, A. V. Static and Dynamic Properties of 0, π , and 0 − π Ferromagnetic Josephson Tunnel Junctions. *Phys. Rev. B* **2008**, *77* (21), 214506. https://doi.org/10.1103/PhysRevB.77.214506.
97. I.O. Kulik. *JETP Lett.* **1965**, *2* (84).
98. J. C. Swihart. *J. Appl. Phys.* **1961**, *32* (461).
99. Boardman, A. D.; Nikitov, S. A.; Waby, N. A. Existence of Spin-Wave Solitons in an Antiferromagnetic Film. *Phys. Rev. B* **1993**, *48* (18), 13602–13606. https://doi.org/10.1103/PhysRevB.48.13602.
100. Bahr, S.; Alfonsov, A.; Jackeli, G.; Khaliullin, G.; Matsumoto, A.; Takayama, T.; Takagi, H.; Büchner, B.; Kataev, V. Low-Energy Magnetic Excitations in the Spin-Orbital Mott Insulator Sr 2 IrO 4. *Phys. Rev. B* **2014**, *89* (18), 180401. https://doi.org/10.1103/PhysRevB.89.180401.
101. Monaco, R.; Costabile, G.; Martucciello, N. Influence of the Idle Region on the Dynamic Properties of Window Josephson Tunnel Junctions. *J. Appl. Phys.* **1995**, *77* (5), 2073–2080. https://doi.org/10.1063/1.358848.
102. Chikara, S.; Korneta, O.; Crummett, W. P.; DeLong, L. E.; Schlottmann, P.; Cao, G. Giant Magnetoelectric Effect in the J_{eff} = 1/2 Mott Insulator Sr_2IrO_4. *Phys. Rev. B* **2009**, *80* (14), 140407. https://doi.org/10.1103/PhysRevB.80.140407.
103. Hu, J. Microscopic Origin of Magnetoelectric Coupling in Noncollinear Multiferroics. *Phys. Rev. Lett.* **2008**, *100* (7), 077202. https://doi.org/10.1103/PhysRevLett.100.077202.
104. Komissinskiy, P.; Ovsyannikov, G. A.; Borisenko, I. V.; Kislinskii, Yu. V.; Constantinian, K. Y.; Zaitsev, A. V.; Winkler, D. Josephson Effect in Hybrid Oxide Heterostructures with an Antiferromagnetic Layer. *Phys. Rev. Lett.* **2007**, *99* (1), 017004. https://doi.org/10.1103/PhysRevLett.99.017004.
105. Barash, Yu. S. Quasiparticle Interface States in Junctions Involving *d* -Wave Superconductors. *Phys. Rev. B* **2000**, *61* (1), 678–688. https://doi.org/10.1103/PhysRevB.61.678.
106. Löfwander, T.; Shumeiko, V. S.; Wendin, G. Andreev Bound States in High- T_c Superconducting Junctions. *Supercond. Sci. Technol.* **2001**, *14* (5), R53–R77. https://doi.org/10.1088/0953-2048/14/5/201.
107. Riedel, R. A.; Bagwell, P. F. Low-Temperature Josephson Current Peak in Junctions with d -Wave Order Parameters. *Phys. Rev. B* **1998**, *57* (10), 6084–6089. https://doi.org/10.1103/PhysRevB.57.6084.
108. Lu, C.; Quindeau, A.; Deniz, H.; Preziosi, D.; Hesse, D.; Alexe, M. Crossover of Conduction Mechanism in Sr_2IrO_4 Epitaxial Thin Films. *Appl. Phys. Lett.* **2014**, *105* (8), 082407. https://doi.org/10.1063/1.4894465.
109. Gor'kov, L.; Kresin, V. Giant Magnetic Effects and Oscillations in Antiferromagnetic Josephson Weak Links. *Appl. Phys. Lett.* **2001**, *78* (23), 3657–3659. https://doi.org/10.1063/1.1377310.
110. Kornev, V. K.; Karminskaya, T. Y.; Kislinskii, Y. V.; Komissinki, P. V.; Constantinian, K. Y.; Ovsyannikov, G. A. Dynamics of Underdamped Josephson Junctions with Non-Sinusoidal Current-Phase Relation. *Phys. C Supercond. Its Appl.* **2006**, *435* (1–2), 27–30. https://doi.org/10.1016/j.physc.2006.01.012.